Geochimica et Cosmochimica Acta 393 (2025) 133–154

Contents lists available at ScienceDirect

Geochimica et Cosmochimica Acta

journal homepage: www.elsevier.com/locate/gca

Bulk silicate Earth-like ^{142}Nd and ^{182}W mantle component sampled by 2.0 Ga Onega Basin picrites, Fennoscandia

I.S. Puchtel [a,*], J.L. Hellmann [a], H. Rizo [b], J. Blichert-Toft [c], A.V. Stepanova [d], A.V. Samsonov [e], R.J. Walker [a]

[a] Department of Geology, University of Maryland, College Park, MD 20742, USA
[b] Department of Earth Sciences, Carleton University, Carleton-Ottawa Geoscience Centre, Ottawa, ON K1S 5B6, Canada
[c] Laboratoire de Géologie de Lyon, CNRS UMR 5276, Ecole Normale Supérieure de Lyon, Lyon, France
[d] Institute of Geology, Karelian Center of the Russian Academy of Sciences, Pushkinskaya 11, Petrozavodsk 185910, Russia
[e] Institute of Geology of Ore Deposits, Petrography, Mineralogy and Geochemistry, Russian Academy of Sciences, Staromonetny 35, Moscow 109017, Russia

ARTICLE INFO

Associate editor: Vinciane Debaille and Oliver Nebel

Keywords:
^{182}Hf-^{182}W and ^{146}Sm-^{142}Nd short-lived radiogenic isotope systems
^{176}Lu-^{176}Hf, ^{147}Sm-^{143}Nd, ^{190}Pt-^{186}Os, and ^{187}Re-^{187}Os long-lived radiogenic isotope systems
Mantle evolution
Highly siderophile elements
Picrites and basalts
Fennoscandian Shield
Onega Basin
Starting mantle plume

ABSTRACT

In order to further evaluate the timing and possible mechanisms responsible for the transition from both positive and negative to no ^{142}Nd and ^{182}W anomalies in the Archean mantle, we obtained ^{142,143}Nd, ^{176}Hf, ^{186,187}Os, ^{182}W isotope and lithophile trace and highly siderophile element (HSE: Os, Ir, Ru, Pt, Pd, and Re) abundance data for mantle plume-derived ~2.0 Ga picrites and an associated differentiated mafic–ultramafic sill from the Onega Basin on the Fennoscandian Shield. The Onega Basin picrites share striking chemical similarities with the modern Kilauea picrites, featuring enrichments in light rare earth elements (LREE; $La/Sm_N = 1.5 \pm 0.2$), depletions in heavy rare earth elements (HREE; $Gd/Yb_N = 2.2 \pm 0.1$), positive high field strength element (HFSE) anomalies ($Hf/Hf^* = 1.2 \pm 0.1$, $Nb/Nb^* = 1.6 \pm 0.1$), and modern bulk silicate Earth (BSE)-like average $W/Th = 0.20 \pm 0.08$ (2SD). Model calculations indicate that the parental picritic magmas were likely derived from 3 % equilibrium batch melting of a LREE-depleted garnet lherzolite PREMA-type mantle source containing a component of recycled oceanic crust.

The ^{147}Sm-^{143}Nd, ^{176}Lu-^{176}Hf, and ^{187}Re-^{187}Os mineral-whole-rock isochron ages constrain precisely the timing of the Onega Basin lava emplacement at ~1974 Ma. The corresponding initial $\varepsilon^{143}Nd = +3.0 \pm 0.5$ and $\varepsilon^{176}Hf = +2.8 \pm 1.2$ values indicate evolution of the Onega mantle source with time-integrated suprachondritic Sm/Nd and Lu/Hf ratios. The lower ε^{176}Hf relative to ε^{143}Nd further implies decoupling of the two lithophile element isotope systems in the source. The initial μ^{186}Os and γ^{187}Os values are suprachondritic at $+4.9 \pm 2.1$ and $+2.9 \pm 0.4$, respectively, indicating evolution of the Onega mantle plume source with time-integrated slightly suprachondritic Pt/Os and Re/Os ratios. The $\mu^{142}Nd = -1.1 \pm 3.3$ (2SD) and $\mu^{182}W = 0.0 \pm 4.8$ (2SD) obtained for the Onega picritic magmas are unresolvable from the modern BSE values, implying that their mantle source had ^{142}Nd and ^{182}W compositions similar to those of the BSE. When considered together, the trace element systematics, suprachondritic Pt/Os and Re/Os ratios, and Hf-Nd isotopic decoupling are best explained in terms of incorporation into the Onega mantle plume source of 10–20 % recycled komatiite-basalt crust aged in the mantle for 1 to 2 Ga. These results provide new evidence that ^{142}Nd and ^{182}W anomalies that were common in the Archean mantle were effectively homogenized by 2.0 Ga ago on the scale of the mantle domains sampled by the Onega Basin magmas. This may have occurred due to the enhanced convective whole-mantle mass and heat transfer facilitated by processes of oceanic crust recycling that may have operated since at least the early Archean.

1. Introduction

Studies of short-lived radiogenic isotope systems such as ^{182}Hf→^{182}W ($t_{1/2}$ = 8.9 Ma: Vockenhuber et al., 2004) and ^{146}Sm→^{142}Nd ($t_{1/2}$ = 103 Ma: Meissner et al., 1987) have contributed to an improved understanding of the global processes that shaped Earth

* Corresponding author.
E-mail address: ipuchtel@umd.edu (I.S. Puchtel).

https://doi.org/10.1016/j.gca.2025.01.013
Received 12 June 2024; Accepted 11 January 2025
Available online 17 January 2025

from planetary accretion and differentiation (e.g., Lee and Halliday, 1995; 1996; Schoenberg et al., 2002; Yin et al., 2002; Kleine et al., 2004) to subsequent mixing (e.g., Jacobsen and Harper, 1996; Harper and Jacobsen, 1992; Caro et al., 2003; Boyet et al., 2003; Boyet and Carlson, 2006). Radiogenic ^{182}W and ^{142}Nd isotope abundance anomalies compared to the present-day bulk silicate Earth (BSE) compositions provide evidence of the survival of vestiges of ancient reservoirs that must have formed during the first, respectively, ~50 and ~500 Ma of Earth's history and, further, that some of these early-formed mantle reservoirs survived for over 2 billion years (e.g., Touboul et al., 2012; Debaille et al., 2013; Puchtel et al., 2018).

Variable in magnitude ^{142}Nd and ^{182}W anomalies have been detected in Archean mantle-derived rocks (e.g., Caro et al., 2006, Touboul et al., 2012, 2014; Rizo et al., 2016; Debaille et al., 2013; Puchtel et al., 2016a, Garcia et al., 2023). By contrast, studies of young mid-ocean ridge basalts (MORB) and ocean island basalts (OIB) indicate that surviving ^{142}Nd anomalies are rare (Horan et al., 2018; Peters et al., 2018, 2021; Hyung and Jacobsen, 2020; Peters et al., 2024). On the other hand, negative ^{182}W anomalies consistently have been reported for OIB, mostly for those with elevated ^{3}He/^{4}He ratios (e.g., Mundl et al., 2017; Peters et al., 2021; Mundl-Petermeier et al., 2019, 2020; Rizo et al., 2019), and for some kimberlites ranging in age from the Archean to the present (Nakanishi et al., 2021), while MORB are characterized by an absence of ^{182}W anomalies (Rizo et al., 2016; Mundl et al., 2017; Peters et al., 2024). When this transition from positive to negligible or negative anomalies occurred, and which mechanism(s) were responsible for this change, remain unclear. Although prior studies have concluded that positive ^{142}Nd and ^{182}W anomalies largely disappeared by the end of the Archean (e.g., Mei et al., 2020, 2023; Tusch et al., 2021; Nakanishi et al., 2023), only few early Proterozoic mafic–ultramafic rocks have been studied so far (e.g., Puchtel et al., 2016b, 2020). To address these issues, we obtained ^{142,143}Nd, ^{176}Hf, ^{182}W, and ^{186,187}Os isotope and lithophile

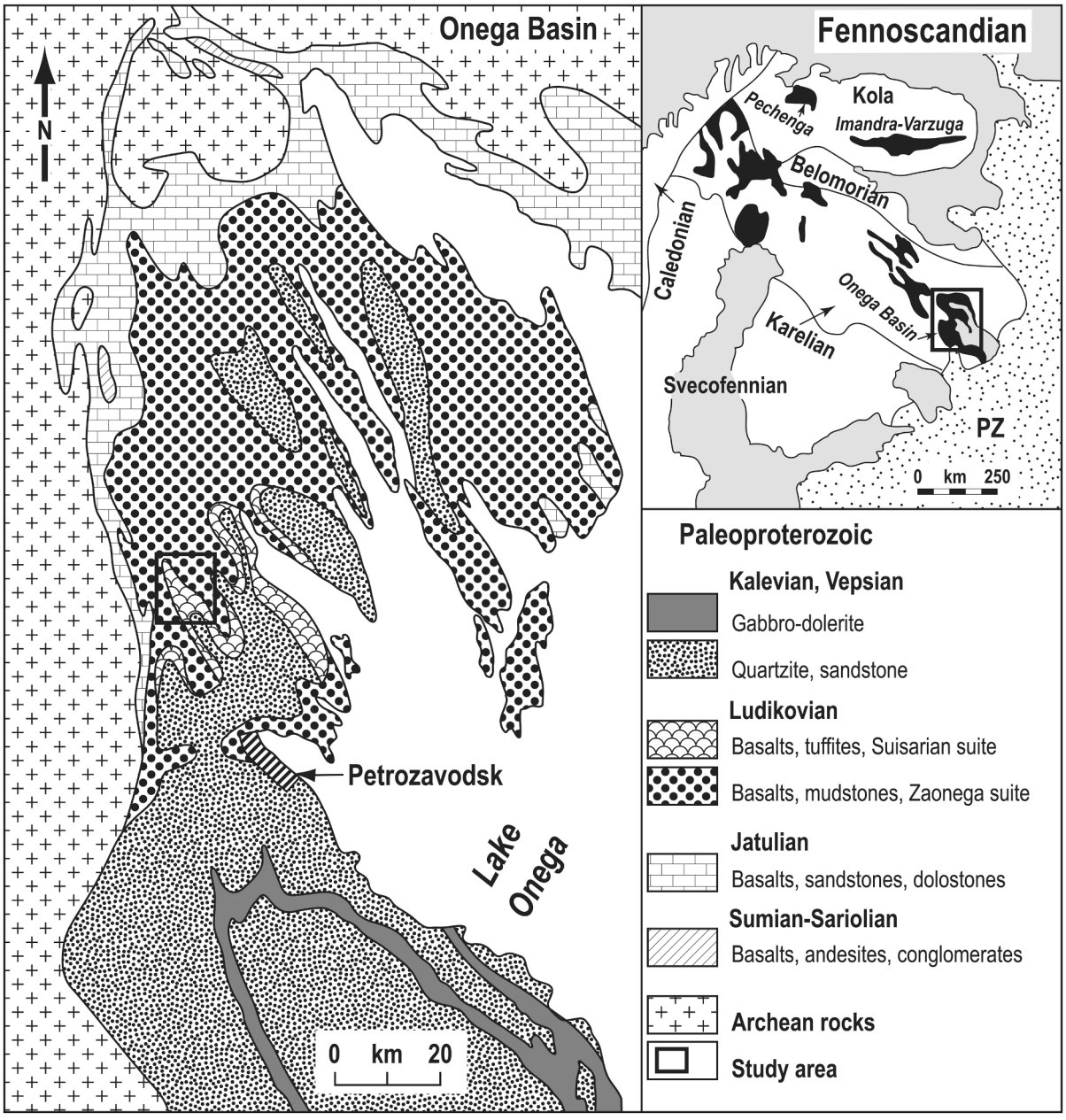

Fig. 1. Geological sketch map of the Onega Basin. Black areas in the inset map reflect the distribution of the Jatulian and Ludikovian rocks on the Fennoscandian Shield.

and siderophile trace element abundance data for ~2.0 Ga picrites and related rocks from the Onega Basin on the Fennoscandian Shield. These rocks were targeted because they (a) have the appropriate age (i.e., 2.0 Ga) to begin to fill the above-mentioned gap in the geological rock record, (b) retained magmatic petrological and chemical features closely resembling those of some modern OIB, and (c) have been argued to be derived from melting in a deep mantle plume (Hanski and Smolkin, 1995; Puchtel et al., 1998).

2. Geological background, samples, and previous studies

The Karelian Province of the Fennoscandian Shield is a typical Archean granite-greenstone terrain covered by Paleoproterozoic volcano-sedimentary sequences (inset map in Fig. 1). The Paleoproterozoic rocks are divided into several stratigraphic units (from bottom to top): the Sumian, Sariolian, Jatulian, Ludikovian, Kalevian, and Vepsian (Gaál and Gorbatschev, 1987; Sokolov, 1987).

The Ludikovian (~2.10–1.92 Ga) sequences (black areas within the inset map in Fig. 1) form several epicontinental basins representing spatially separated relicts of a presumably once continuous cover deposited over the Jatulian sequences. These basins attain thicknesses of 4,500 m and cover a total area of >50,000 km^2 at the present erosion level (Sokolov, 1987). The uneroded sequences were likely thicker and areally much more extensive, covering an area in excess of 500,000 km^2, with the volume of erupted magma as high as 10^6 km^3. In the Kola Province, these basins include the Pechenga-Imandra-Varzuga volcanic belt containing massive volumes of high-Ti komatiites, picrites, and basalts (Hanski and Smolkin, 1989, 1995; Hanski et al., 1990; Hanski, 1992, Arzamastsev et al., 2020). In the Karelian Province, the Ludikovian sequences include basaltic and picritic lavas of the Onega Basin (Svetov, 1979; Puchtel et al., 1998).

Based on the large volumes and presumably short time span of magma emplacement, Hanski (1992), Hanski and Smol'kin (1995), and Puchtel et al. (1998) suggested that the Ludikovian basins represent relicts of an ancient continental flood basalt province (CFBP), which they named the Onega Plateau, and that parental picritic magmas of the Onega Plateau volcanic sequences were derived from a starting mantle plume ~2000 km in diameter that impinged on the lithospheric mantle and passed through the granitic crust *en route* to the surface ~2.0 Ga ago.

This study focuses on the Ludikovian rocks within the SE fragment of the Onega Plateau exposed on the NW shore of Lake Onega and referred to as the Onega Basin (inset map in Fig. 1). In the Onega Basin, the Ludikovian consists of the lower Zaonega and the upper Suisarian Formations (Fms). The Zaonega Fm has a thickness of up to 1,800 m and is composed of submarine volcanic, volcaniclastic, and sedimentary sequences, including carbonaceous rocks, mudstones, dolomites, basalts, and basaltic tuffs (Melezhik et al., 2013). The Suisarian Fm is up to 700 m thick and consists of basaltic tuffs, tuff-agglomerates, hyaloclastites, pillowed basalts, and picrites emplaced at shallow-water depths. The rocks were metamorphosed under prehnite-pumpellyite to lower greenschist facies conditions.

Puchtel et al. (1998) reported combined whole-rock-mineral Sm-Nd and Pb-Pb isochron ages for the Konchozero sill, considered to be a feeding magma chamber to the Suisarian picrites and basalts, of 1975 ± 24 Ma and 1980 ± 57 Ma, respectively. These ages were interpreted to reflect the time of emplacement of the Suisarian Fm lavas. Consistent with these data, Puchtel et al. (1999) obtained a Re-Os isochron age of 1969 ± 18 Ma using a combination of whole-rock samples and chromite separates, and Stepanova et al. (2024) reported a SHRIMP U-Pb concordant zircon age of 1963 ± 6 Ma for the gabbroic part of the Konchozero sill, providing precise constraints on the timing of the Suisarian volcanic activity.

Additionally, a positive initial $\varepsilon^{143}Nd$ value of +3.2 ± 0.2 and a relatively unradiogenic μ_1 (the time-integrated $^{238}U/^{204}Pb$ ratio of the source) of 8.57 ± 0.03 were reported by Puchtel et al. (1998), along with an initial $\gamma^{187}Os$ value of +0.77 ± 1.7 (Puchtel et al, 1999).

This study is focused on the picritic lavas and the differentiated Konchozero mafic–ultramafic sill located within the Angozero area, ~40 km NW of the city of Petrozavodsk (Fig. 1). The sampling locations designated as A, B, and C, both on the map and in the stratigraphic cross-sections, are illustrated in Figs. 2 and 3. The Angozero area is composed of the Zaonega and overlying Suisarian Fms rocks. The former is represented by aphyric and plagioclase-phyric basalts and tuffs intruded by the Konchozero sill. The Suisarian Fm consists of intercalated pyroxene-olivine-phyric picritic and basaltic lavas and tuffs. The thickness of the Suisarian Fm in the area is >420 m (Svetov, 1979).

Six pyroxene-olivine-phyric picritic samples collected from surface outcrops across a ~200 m section (Fig. 2C) were selected for this study. These rocks are green-gray in outcrop consisting of variable amounts of tabular and prismatic pyroxene grains and serpentine pseudomorphs after platy olivine grains set in a fine-grained pyroxene-plagioclase matrix. The flows are generally uniform in texture and vary in thickness from a few meters to a few tens of meters. The weak zoning that is sometimes observed in these flows is due to the presence of thin chilled zones at the bottom and amygdaloidal zones at the top of the flows. The amygdules are usually small and rounded and are concentrated directly beneath the upper chilled crust. Brecciated textures sometimes observed at the top of lava flows are characterized by the presence of fragments of chilled upper crust cemented by lava material.

The Konchozero sill is a differentiated body that ranges in thickness from a few tens of meters near the flanks to ~150 m in the central portion (Figs. 2 and 3). The lower chilled margin is a few meters thick and is composed of altered glassy rock with minor (10–12 %) crystalline material, including small platelets of well-preserved pyroxene and tabular olivine grains completely replaced by serpentine. The lower chilled zone grades upward into the olivine-pyroxene cumulate zone, which is up to 100 m thick. The transition is accompanied by an increase in the abundance and grain size of pyroxene and olivine. The olivine-pyroxene cumulate zone is composed of euhedral olivine grains Fo_{81-83} that are partially to completely replaced by serpentine, well preserved augite (X_{Mg} = 0.85–0.87) grains, up to 5 mm in size, and minor chromite, in a matrix of fine-grained olivine, augite, chromite, and ilmenite. Chromite occurs as small rounded inclusions, 30–50 μ m in size, in the euhedral olivine and augite grains, and as larger, 100–300 μ m in size, euhedral grains in the matrix (***Supplementary Fig. S1***). The olivine abundance in the olivine-pyroxene cumulate zone increases upward from the lower to the middle cumulate zone, and then decreases again in the upper cumulate zone. The upper cumulate zone is overlain by a medium- to coarse-grained gabbro zone that is ~10 m thick and composed of euhedral grains of plagioclase (75–90 %) and augite (25–10 %). The upper chilled margin of the sill is composed of a fine-grained rock consisting mostly of small prismatic augite grains and subordinate amounts of serpentinized tabular olivine grains in a fine-grained pyroxene-plagioclase matrix.

The Konchozero sill samples selected for this study were collected from two localities (A and B) ~2 km apart (Figs. 2 and 3), from the lower chilled margin (sample 689–1), lower cumulate zone (9705, 9112/3, 689–2, 689–3), middle cumulate zone (9704, 689–4, 689–5, 689–6), upper cumulate zone (9702), gabbro (689–7), and upper chilled margin (9112/1, 9112/2, 9701).

For this study, we used existing whole-rock powders but also prepared new powders of whole-rock samples. For the Angozero picritic lava samples and Konchozero sill samples from Section A, we made new powders from the unprocessed rock material remaining from Puchtel et al. (1998, 1999) to avoid the potential effects of contamination with metal during sample powder preparation in those earlier studies. Several additional Angozero picrite samples (9108, 9109, 9109/1), collected but not analyzed by Puchtel et al. (1998, 1999), were also powdered using metal-free equipment and included in this study. For the samples from Section B of the Konchozero sill (689–1 through 689–7), we used the sample powders from Nicklas et al. (2019), as these powders had been prepared using metal-free equipment.

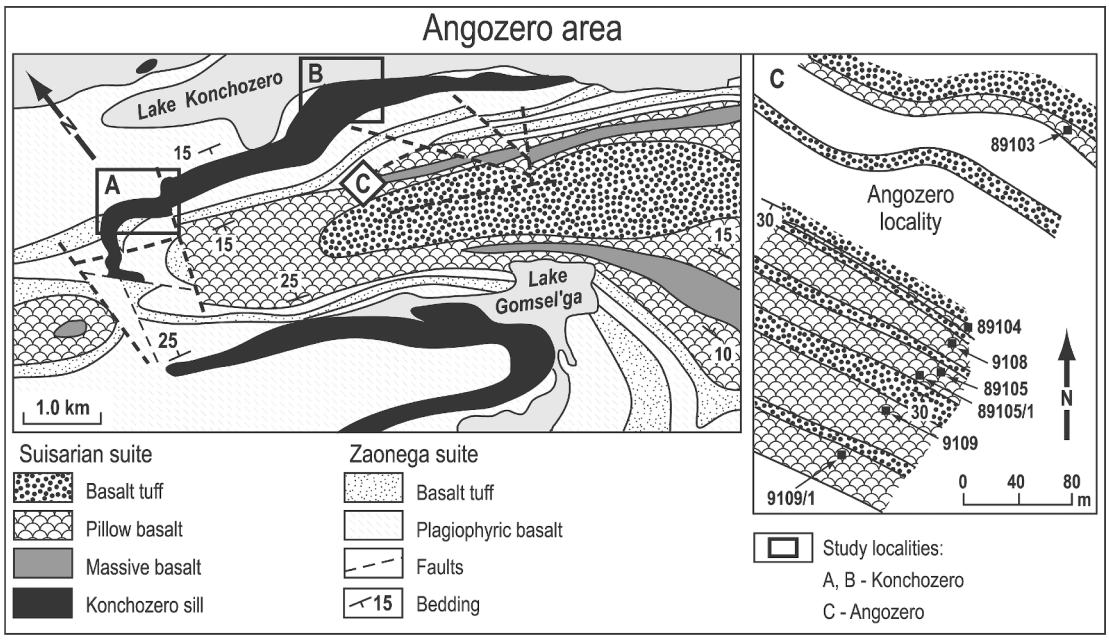

Fig. 2. Geological sketch maps of the Angozero area with the Konchozero (A and B) and Angozero (C) study localities and locations of the samples analyzed.

3. Analytical techniques

Analytical details for the ^{142,143}Nd, ^{186,187}Os, ^{176}Hf, and ^{182}W isotopic and trace element and W abundance analyses have been previously published (Puchtel et al., 2016b, 2018, 2020, 2022a; Garçon et al., 2018); here, we provide only a brief overview of the techniques used in this study. For the complete outline, the reader is referred to the online ***Supplementary Materials*** section.

3.1. Sample preparation and mineral separation

Hand specimens 0.5–1.0 kg in weight collected from surface outcrops were cut into 1–2 cm thick slabs using a diamond saw to remove any signs of alteration. The slabs were then abraded on the cut surfaces using SiC sandpaper to remove saw marks, rinsed in de-ionized water, dried, and crushed in an alumina-faced jaw crusher. A 200 g aliquot of crushed sample was ground in an alumina-faced disk mill and used for the analyses.

The clinopyroxene and chromite separates were obtained at the Institute of Geology of Ore Deposits, Petrology, Mineralogy and Geochemistry (IGEM), Russian Academy of Sciences in Moscow, using a combination of heavy liquid, magnetic separation, and handpicking techniques.

3.2. Major, minor, and lithophile trace element abundances

Major and minor element analyses were carried out at Franklin and Marshall College on fused glass discs using a Phillips 2404 XRF vacuum spectrometer following the protocol of Mertzman (2000). The typical accuracy and precision of the analyses was ~2 % (2SD) relative for major elements present in concentrations greater than 0.5 wt. %, and ~5 % relative for the rest of the major and the minor elements, as determined *via* analysis of the USGS Geochemical Reference Materials (GRM) BIR-1 and BCR-1 as unknowns (Supplementary ***Table S1***).

Lithophile trace element abundances were determined at the *Isotope Geochemistry Laboratory and Plasma Laboratory* (*IGL/PL*), University of Maryland College Park (UMCP), using the standard addition solution inductively-coupled plasma mass-spectrometry technique (SA ICP-MS) following the protocols outlined in Nicklas et al. (2016) and Puchtel et al. (2016b). The accuracy and precision of the analyses were evaluated on the basis of analyses of USGS GRM BIR-1 and BCR-1 (Supplementary ***Table S2***) and were better than 2 % (2SD) relative for all elements.

3.3. Re-Os and Pt-Os isotopic compositions and HSE abundances

To obtain the Re-Os isotopic and HSE abundance data, the analytical protocols detailed in Puchtel et al. (2016b, 2020) were followed. Osmium isotopic measurements were done via negative thermal ionization mass spectrometry (N-TIMS: Creaser et al., 1991); all samples were analyzed using a secondary electron multiplier (SEM) detector of a *ThermoFisher Triton* mass-spectrometer at the *IGL*. The in-run precision of measured ^{187}Os/^{188}Os ratios for all samples was between 0.03 % and 0.06 % relative (2SE). The initial γ^{187}Os values were calculated as the per cent deviations of the ^{187}Os/^{188}Os ratios in samples at the time defined by the Re-Os isochron, relative to that in the chondritic reference of Shirey and Walker (1998) at that time. The average chondritic Os isotopic composition at the time defined by the isochron was calculated using the ^{187}Re decay constant $\lambda = 1.666 \times 10^{-11}$ year^{-1}, an early Solar System initial ^{187}Os/^{188}Os = 0.09531 at 4.558 Ga, and ^{187}Re/^{188}Os = 0.40186 (Smoliar et al., 1996; Shirey and Walker, 1998).

The measurements of Ru, Pd, Re, Ir, and Pt abundances were performed using Faraday cups of a *ThermoFisher Neptune Plus* MC ICP-MS at the *PL*. The external precision of the analyses was estimated on the basis of standard measurements performed during the period of the analytical campaign to be ^{185}Re/^{187}Re = 0.3 %, ^{99}Ru/^{101}Ru = 0.3 %, ^{191}Ir/^{193}Ir = 0.2 %, ^{194}Pt/^{196}Pt = 0.1 %, and ^{105}Pd/^{106}Pd = 0.1 % relative (2SD).

The average total analytical blank (TAB) measured during the present analytical campaign was (in pg): Ru = 2.8, Pd = 24, Re = 1.1, Os = 0.74, Ir = 0.16, and Pt = 95 (N = 12). The average TAB constituted < 0.10 % for Os, Ir, and Ru, <1.1 % for Re, <2% for Pt and < 0.12 % for Pd of the total amount of element analyzed. The uncertainties on the abundances for each element in the samples are, thus, those cited above, assuming 100 % variation in the TAB. The reported uncertainty on the Re/Os ratio was calculated by combining the estimated uncertainties on the Re and Os abundances for each sample.

The accuracy of the Re-Os isotope and HSE abundance data was assessed by comparing the results for the reference materials IAG MUH-1 (Austrian harzburgite), IAG OKUM (ultramafic komatiite), and NRC TDB-1 (Diabase PGE Rock Material) obtained at the *IGL* with the

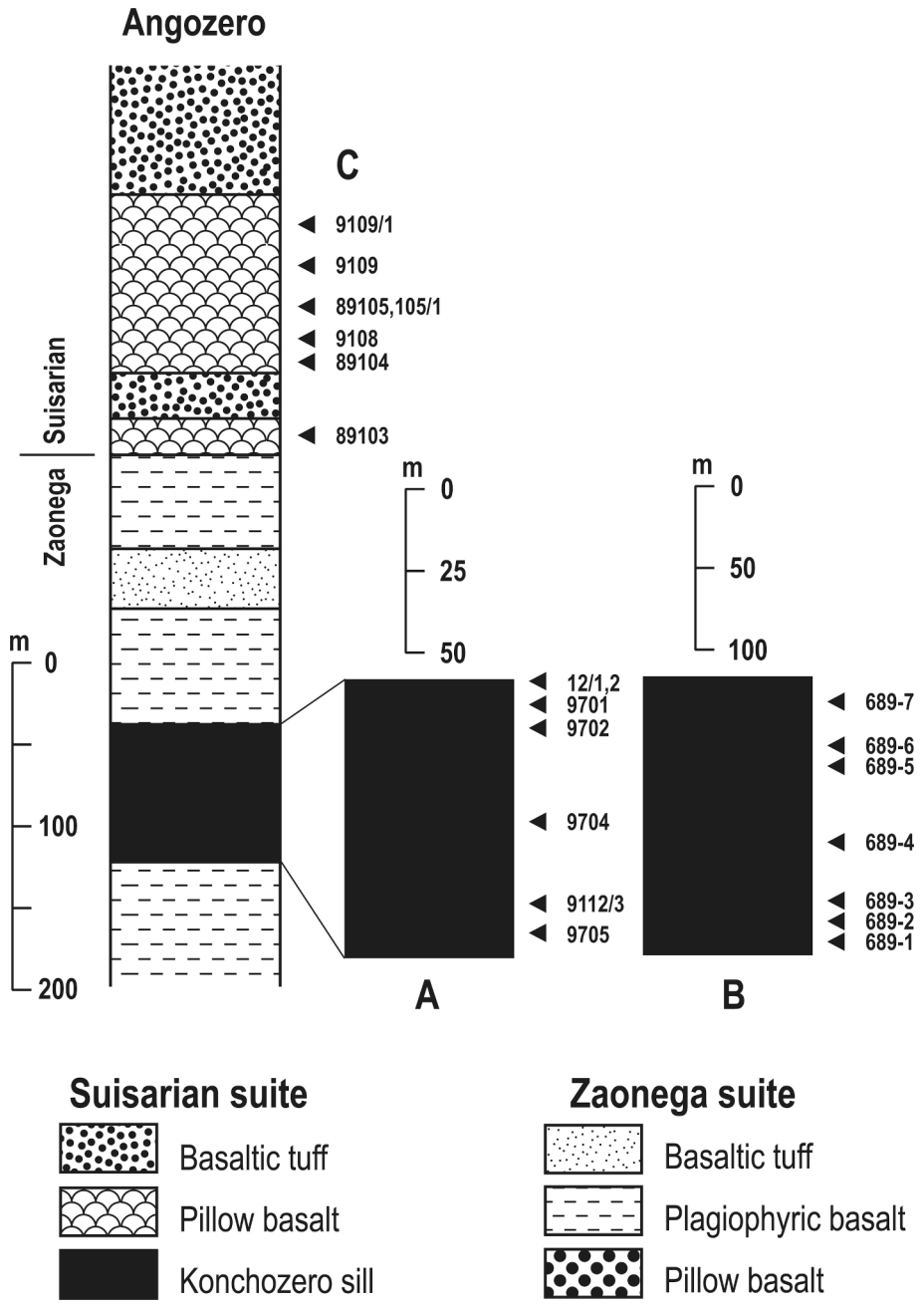

Fig. 3. Stratigraphic cross-section through the Angozero study area and location of the samples analyzed.

reference values. Concentrations of all HSE and Os isotopic compositions obtained at the *IGL* are within the uncertainties of the certified reference values for these reference materials (Supplementary ***Table S3***).

For the Pt-Os isotopic study, the protocol of Puchtel et al. (2016b, 2020) was followed. The high-precision measurements of the $^{186}Os/^{188}Os$ and $^{187}Os/^{188}Os$ ratios were performed by N-TIMS in static mode on a *ThermoFisher Triton* mass spectrometer at the *IGL*. The mean of the *Johnson Matthey* Os standard runs during the period of data collection was 0.001305 ± 1 for $^{184}Os/^{188}Os$, 0.1198454 ± 14 (±11 ppm) for $^{186}Os/^{188}Os$, and 0.113783 ± 6 for $^{187}Os/^{188}Os$ (2SD, $N = 16$); these uncertainties were used to assess the true uncertainty on the measured $^{186}Os/^{188}Os$ and $^{187}Os/^{188}Os$ ratios for the individual samples. To calculate the initial $^{186}Os/^{188}Os$ ratios, the Pt/Os ratios obtained from the spiked runs and the ^{190}Pt decay constant $\lambda = 1.477 \times 10^{-12}$ $year^{-1}$ (Walker et al., 1997; Begemann et al., 2001) were used. Initial $\mu^{186}Os$ values were calculated as parts per million (ppm) deviation of the $^{186}Os/^{188}Os$ ratio of the sample at 1974 Ma relative to that in the chondritic reference of Brandon et al. (2006) at the same age and using a Solar System initial $^{186}Os/^{188}Os = 0.1198269$ at $T = 4567$ Ma and $^{190}Pt/^{188}Os = 0.00174$.

3.4. Tungsten isotopic compositions and abundances

The W isotope analyses were carried out at the *IGL/PL* and at the *Isotope Geochemistry and Geochronology Research Centre (IGGRC)*, Carleton University, Ottawa, Canada.

Research groups that are currently obtaining ^{182}W data utilize either N-TIMS or MC ICP-MS, and rarely both. In the N-TIMS studies, W isotopes are measured as negative trioxides, while in the MC ICP-MS studies, W is measured in its metal form. A discrepancy between both techniques has sometimes been reported (e.g., Kruijer and Kleine, 2018) and that discrepancy has been argued to result from ^{183}W deviations

usually obtained during MC ICP-MS analyses. These deviations then require correction that would be applied to all W isotopes. In this study, given that both instruments were available to us, we decided to measure the Onega samples using both instruments, leading to a more robust dataset. It is worth noticing that we did not detect any ^{183}W deviations and, thus, no further corrections were applied to the data.

At the *IGL/PL*, W isotopic compositions were measured using either a *ThermoFisher Triton* TIMS in negative mode using a 2-line multi-static acquisition protocol and following a slightly modified technique of Archer et al. (2017), or a *ThermoFisher Neptune Plus* MC ICP-MS. For N-TIMS, W was loaded onto outgassed, zone-refined Re filaments, together with a La-Gd activator solution. Tungsten was measured as triple oxide anions (WO_3^-), where oxide production is facilitated by the activator and O_2 bleed into the TIMS source (pressure ca. 1.2×10^{-7} mbar). The $^{186}W^{16}O_2^{18}O$ and $^{187}Re^{16}O_2^{18}O$ oxides were measured on every line of the acquisition protocol using 10^{12} Ω amplifiers, thus, allowing per-integration oxide interference corrections. The rest of the isotope ratios were measured using 10^{11} Ω amplifiers. The effects of instrumental mass-fractionation were corrected for using $^{186}W/^{183}W = 1.98590$ or $^{186}W/^{184}W = 0.92767$ (Völkening et al., 1991; Archer et al., 2017). All data are reported in $\mu^{182}W$ and $\mu^{183}W$ terms, which are parts per million (ppm) deviations of $^{182}W/^{184}W$ and $^{183}W/^{184}W$, respectively, in a given sample from those of the *Alfa Aesar* W standard solution. Uncertainties on $\mu^{182}W$, based on the 2SD uncertainty of the *Alfa Aesar* standard runs during each analytical session, were between ±2.2 and ±4.3 ppm.

For the MC ICP-MS measurements, samples were introduced using a Cetac Aridus 3 desolvator and a Savillex C-flow nebulizer at an uptake rate of 50 μL/min. Total ion beam intensities of ~3×10^{-10} A were obtained for a ~50 ppb W solution, using Jet sampler and X skimmer cones. Each measurement consisted of 60 s baseline integrations, followed by 200 isotope ratio measurements of 4.2 s each. Each sample analysis was bracketed by measurements of an *Alfa Aesar* W standard solution (*Specpure*, Lot No. 211576G), and both the samples and standards were analyzed at similar ion beam intensities. Isobaric Os interferences on ^{184}W and ^{186}W were monitored on mass ^{188}Os and corrections were negligible for all samples. Instrumental mass bias was corrected relative to $^{186}W/^{183}W = 1.98590$ or $^{186}W/^{184}W = 0.92767$ (Völkening et al., 1991; Archer et al., 2017) using the exponential law. Results are reported as the means of solution replicates ($N = 9$–11), with their corresponding 95 % confidence intervals. In this study, we used $^{186}W/^{184}W$-normalized ^{182}W data to avoid normalizations involving ^{183}W, which can be biased by a small analytical artifact resulting from odd-even isotope effects (Willbold et al., 2011; Kruijer et al., 2012; Cook and Schönbächler, 2016; Budde et al., 2022).

At the *IGGRC*, W isotopic compositions were measured by N-TIMS on a *ThermoFisher Triton* mass-spectrometer using the protocol similar to that utilized at *IGL/PL*. Uncertainty on $\mu^{182}W$, based on the 2SD uncertainty of the *Alfa Aesar* W standard runs during the analytical session, was ±4.0 ppm.

Tungsten abundances were determined by isotope dilution at the *IGL/PL,* and duplicate measurements for selected samples were performed at the *IGGRC*. Concentrations were measured at both laboratories using their *ThermoFisher Neptune Plus* MC ICP-MS. The average TAB was ≤ 230 pg, constituting < 1 % of the total element analyzed. Accuracy of W abundance determinations were monitored by comparing the measurements of USGS GRM BHVO-2 and BCR-2, which yielded similar abundances to those reported by Jochum et al. (2016). Typical uncertainties on the concentrations were ~0.5 % relative.

3.5. ^{147}Sm-^{143}Nd isotopic compositions and Sm and Nd abundances

The Sm-Nd isotopic data were obtained at the *IGL/PL* following the protocol of Puchtel et al. (2020, 2022a). Measurements of Nd isotopic compositions were performed on Faraday cups of the *ThermoFisher Neptune Plus* ICP-MS in static mode using 10^{11} Ω amplifiers on all masses, except for ^{147}Sm, on which a 10^{13} Ω amplifier was used. The in-run precision of the measured $^{143}Nd/^{144}Nd$ ratio for both the samples and standards was between ±5 and ±7 ppm (2SE). During the course of the present analytical campaign, the external precision of the 50 ppb AMES Nd standard solution measurements for $^{143}Nd/^{144}Nd$ was ±10 ppm (2SD). The average $^{143}Nd/^{144}Nd$ ratio measured for the AMES Nd standard during each analytical session was used to calculate the instrumental mass-bias coefficient for correction of the measured $^{143}Nd/^{144}Nd$ in the samples using the long-term average $^{143}Nd/^{144}Nd$ value of 0.512152 ± 2 (2SD) measured precisely on the *IGL ThermoFisher Triton* using a multi-dynamic routine (Puchtel et al., 2016a,b, 2018).

In order to assess the accuracy of the analyses, several separate powder aliquots of USGS GRM BCR-1 and BIR-1 were processed and analyzed using the same analytical protocol (Supplementary ***Table S4***). The measured $^{143}Nd/^{144}Nd$ ratios for both GRM are identical, within their respective uncertainties, to the GeoRem preferred values, as well as to the average high-precision value for BCR-1 (0.512645 ± 1, 2SD) obtained on the *IGL ThermoFisher Triton* using a multi-dynamic routine (Puchtel et al., 2018).

Measurements of the spiked Sm isotopic compositions were also performed on the Faraday cups of the *ThermoFisher Neptune Plus* MC ICP-MS in static mode using 10^{11} Ω amplifiers on all masses except for ^{155}Gd, on which a 10^{13} Ω amplifier was used. The uncertainty on the Sm/Nd ratio in the samples analyzed was conservatively estimated on the basis of replicate analyses of the USGS GRM BCR-1 and BIR-1 to be 0.20 % relative (2SD).

For the isochron calculations, ISOPLOT 3.00 (Ludwig, 2003) and the ^{147}Sm decay constant $\lambda = 6.54 \times 10^{-12}$ year^{-1} (Lugmair and Marti, 1978) were used. The initial $\varepsilon^{143}Nd$ values were calculated based on the present-day parameters of the Chondritic Uniform Reservoir (CHUR): $^{147}Sm/^{144}Nd = 0.1967$ (Jacobsen and Wasserburg, 1980) and $^{143}Nd/^{144}Nd = 0.512638$ (Hamilton et al., 1983).

3.6. ^{142}Nd compositions

The high-precision Nd isotopic data were acquired at the *Advanced Research Complex* (*ARC),* U. of Ottawa, Canada. Neodymium purification involved a four-step chemical separation method, following the protocols similar to those described in Garçon et al. (2018). The LREE were isolated from the whole-rock matrix using AG50W-X8, 200–400 mesh cation-exchange resin. Subsequently, Ce was removed from the LREE fraction by dissolving the cuts in HNO_3 + $NaBrO_3$ and passing them through a column filled with 100–150 μm LnSpec resin. The added Na and Br from the $NaBrO_3$ were then removed using AG50W-X8 cation-exchange resin. Finally, Nd was purified using thin columns filled with 20–50 μm LnSpec resin. Neodymium recovery in this procedure was better than 85 %.

Neodymium isotope measurements were conducted on a *Thermo-Scientific Triton* TIMS at the *ARC*. Samples were loaded into outgassed zone-refined 99.999 % double-assembly Re filaments. Neodymium ratios were obtained using a 2-step dynamic routine, which provides static measurements of all Nd isotope ratios, and dynamic measurements of the $^{142}Nd/^{144}Nd$ ratio. Cerium and Sm isobaric interferences were monitored and corrected for via measurements of the 140 and 147 masses, and $^{140}Ce/^{144}Nd$ and $^{147}Sm/^{144}Nd$ ratios were always lower than 1×10^{-5}. Each Nd isotope measurement comprises 600 ratios measured in 24 blocks of 25 cycles each, with integration times of 8.39 s per cycle, background measurements of 30 s between each block, and no amplifier rotation. Ratios were corrected for instrumental mass fractionation using the exponential law and a $^{146}Nd/^{144}Nd$ ratio of 0.7219. The JNdi-1 Nd standard, which was measured during the same analytical session, yielded an average $^{142}Nd/^{144}Nd = 1.141833 \pm 0.000004$ (2SD, N = 4), which defines the exernal reproducibility of the measurements of 3.7 ppm on the $^{142}Nd/^{144}Nd$ ratio. The $^{142}Nd/^{144}Nd$ values are reported in $\mu^{142}Nd$ terms, which refer to deviations in ppm of $^{142}Nd/^{144}Nd$ in samples relative to the JNdi-1 Nd average.

3.7. Lu-Hf isotopic compositions and abundances

The Lu-Hf concentration and isotopic measurements were carried out at the École Normale Supérieure de Lyon (*ENSL*), France. The sample dissolution procedure, employing Parr bombs and a mixed >98 % pure ^{176}Lu-^{180}Hf spike, and the Lu and Hf separation protocols that were used are those described in Blichert-Toft et al. (1997), Blichert-Toft (2001), and Blichert-Toft and Puchtel (2010). Lutetium and Hf isotopic compositions were measured using the *Nu Plasma 500 HR* multi-collector ICP-MS coupled with a *DSN-100* desolvating nebulizer following the protocols of Blichert-Toft et al. (1997; 2002). Hafnium isotopic ratios were normalized for instrumental mass-fractionation relative to ^{179}Hf/^{177}Hf = 0.7325 using the exponential law. The JMC-475 Hf standard was analyzed every two samples and gave, during the present single analytical session, an average ^{176}Hf/^{177}Hf = 0.282164 ± 0.000010 (2SD; $N = 8$), which represents the external reproducibility of the Hf isotopic analyses (35 ppm). Since the mean ^{176}Hf/^{177}Hf value obtained for the JMC-475 Hf standard is identical, within the quoted uncertainties, to the accepted value of 0.282163 ± 0.000009 (Blichert-Toft et al., 1997), no further corrections were applied to the data. We used the uncertainty obtained from the external reproducibility of the Hf standard as the uncertainty on the Hf isotopic composition for the isochron calculations. The uncertainty on the Lu/Hf ratio was 0.2 % and this was the value we used for the isochron calculations for all samples. Total analytical blanks were < 20 pg for both Lu and Hf.

For the isochron calculations, ISOPLOT 3.00 (Ludwig, 2003) and the ^{176}Lu decay constant of 1.867 × 10^{-11} year^{-1} (Scherer et al., 2001; Söderlund et al., 2004) were used. The ε^{176}Hf values were calculated as parts per 10,000 deviation of the ^{176}Hf/^{177}Hf in the sample at the time of lava emplacement from the chondritic reference at that time (with the Solar System initial values of ^{176}Lu/^{177}Hf = 0.0336 and ^{176}Hf/^{177}Hf = 0.282785: Bouvier et al., 2008).

4. Results

4.1. Major, minor, and trace element abundance data

The chemical compositions of the rocks are listed in Tables 1 and 2 and plotted on MgO variation diagrams in Fig. 4a,b and as BSE-normalized values in Fig. 5. The MgO abundances vary between 13.7 and 20.7 wt% in the Angozero picrites and between 7.05 and 31.5 wt% in the Konchozero differentiated sill. In the Konchozero sill, the MgO abundances decrease from 8.96 wt% in the upper chilled margin to 7.05 wt% in the gabbro layer, and then increase to 21.7 wt% in the upper olivine-pyroxene cumulate zone and to 31.5 wt% in the lower third of the pyroxene-olivine cumulate zone.

The major and trace element data for the Angozero picrite and the Konchozero sill samples plot essentially on the same linear trends for all elements except W, for which the picrites plot somewhat above the general trend and exhibit more scatter. The Konchozero mafic–ultramafic rocks define well-constrained linear trends with negative slopes for incompatible elements; these trends intersect the MgO axes at ~43 wt% MgO for all elements except Sc, for which the intercept is at ~70 wt% MgO. Since Sc is moderately compatible in clinopyroxene ($D_{Sc}^{Cpx-Melt} = 2.5$: Norman et al., 2005), it is likely that this higher MgO intercept is due to the presence of clinopyroxene on the liquidus, as is also indicated by the petrographic data and consistent with previous findings of Puchtel et al. (1998). These authors calculated that the fractionating mineral assemblage consisted of olivine and clinopyroxene in the proportions 80:20. On the basis of the correlations between MgO and elements incompatible with clinopyroxene, Puchtel et al. (1998) calculated that the emplaced Konchozero sill magma contained between 8 and 10 wt% MgO, which is similar to the composition of the upper chilled margin of the sill of ~9.0 wt% MgO. However, no primary olivine was found in either the picrites or the Konchozero sill rocks by Puchtel et al. (1998) preventing a more accurate and precise calculation of the MgO content of the emplaced magma. More recently, Nicklas et al. (2019) studied samples from a different cross-section of the sill (area B in Fig. 3) and reported an average MgO content of the

Table 1
Major (wt. %) and minor (ppm) element abundances in the Angozero picrites and Konchozero sill rocks.

Angozero picrites							
Sample No.	**89103**	**89104**	**89105**	**89105/1**	**9108**	**9109**	**9109/1**
SiO_2	46.6	48.2	46.7	47.6	46.2	47.7	48.5
TiO_2	1.33	1.59	1.89	1.94	1.52	1.77	1.77
Al_2O_3	7.44	10.34	10.8	11.2	8.48	10.2	9.99
Fe_2O_3	13.4	13.6	14.4	14.9	13.5	13.7	12.7
MnO	0.188	0.188	0.182	0.172	0.221	0.179	0.178
MgO	20.7	16.0	14.9	14.0	20.5	16.2	13.7
CaO	9.87	7.92	8.63	7.58	9.08	8.06	10.3
Na_2O	0.126	1.34	1.35	1.76	0.011	1.32	1.87
K_2O	0.016	0.313	0.348	0.350	0.011	0.378	0.577
P_2O_5	0.109	0.151	0.203	0.183	0.169	0.200	0.210
LOI	4.92	4.58	4.05	4.40	4.80	4.50	4.62
Cr	2744	1451	1328	1205	1294	1177	1116
Ni	1228	838	703	600	1008	760	543

Konchozero sill rocks														
Sample No.	**9112/1**	**9112/2**	**9701**	**689-7**	**9112/3**	**9702**	**9704**	**9705**	**689-1**	**689-2**	**689-3**	**689-4**	**689-5**	**689-6**
SiO_2	50.2	49.3	50.6	44.7	43.7	48.6	43.9	42.9	45.9	43.2	42.9	42.4	43.1	43.2
TiO_2	1.94	1.90	2.16	1.58	0.836	1.96	0.867	0.856	1.37	0.804	0.829	0.749	0.740	0.811
Al_2O_3	14.0	14.0	13.8	17.2	4.65	11.9	5.09	4.54	8.12	4.60	4.70	4.69	4.24	4.82
Fe_2O_3	9.69	10.1	10.7	8.02	14.2	11.8	13.8	14.4	14.6	14.4	14.3	14.1	14.2	14.3
MnO	0.197	0.197	0.151	0.181	0.185	0.178	0.195	0.197	0.260	0.201	0.200	0.205	0.194	0.202
MgO	8.96	8.39	7.72	7.05	29.2	13.5	29.1	30.1	21.7	30.5	30.4	31.0	31.5	29.4
CaO	11.2	12.0	9.59	19.9	6.39	8.25	6.19	6.26	7.57	5.57	5.83	5.99	5.20	6.57
Na_2O	3.19	3.45	4.39	0.61	0.206	2.18	0.076	0.077	0.100	0.080	0.100	0.090	0.094	0.108
K_2O	0.232	0.300	0.495	0.384	0.065	1.17	0.065	0.066	0.023	0.097	0.090	0.107	0.136	0.112
P_2O_5	0.148	0.176	0.226	0.158	0.054	0.199	0.087	0.077	0.136	0.080	0.089	0.101	0.073	0.074
LOI	3.54	3.37	3.40	2.57	7.95	5.30	7.30	7.95	6.11	9.09	8.19	7.74	7.61	7.70
Cr	447	456	384	189	2143	730	1903	1976	1467	2045	2181	2197	2306	2197
Ni	217	193	165	127	1506	504	1559	1689	1083	1496	1692	1559	1552	1442

Table 2
Trace element abundances (ppm) in the Angozero picrites and Konchozero sill rocks.

Angozero picrites							
Sample No.	**89103**	**89104**	**89105**	**89105/1**	**9108**	**9109**	**9109/1**
Cu	191	279	294	296	202	280	274
Sc	28.1	29.9	33.7	32.7	28.3	32.9	31.3
Y	13.0	17.6	19.3	20.5	13.9	18.0	19.5
Zr	77.9	112	120	118	83.5	107	119
Nb	9.13	14.0	15.1	15.2	10.1	13.8	15.1
La	6.43	9.28	11.0	11.2	7.25	9.41	11.8
Ce	16.7	21.6	25.0	24.4	17.4	21.3	24.7
Pr	2.31	3.52	3.91	3.72	2.55	3.37	3.83
Nd	10.8	16.2	17.7	17.6	12.5	15.1	17.8
Sm	2.77	4.08	4.73	4.70	3.03	4.18	4.59
Eu	0.750	1.29	1.53	1.54	0.820	1.26	1.48
Gd	3.12	4.36	4.92	5.03	3.19	4.21	4.94
Tb	0.427	0.644	0.755	0.771	0.485	0.638	0.722
Dy	2.50	3.77	4.19	4.37	2.78	3.66	4.16
Ho	0.457	0.712	0.809	0.809	0.499	0.705	0.750
Er	1.19	1.85	2.00	2.13	1.32	1.82	1.98
Tm	0.160	0.251	0.282	0.282	0.177	0.246	0.268
Yb	1.08	1.53	1.69	1.76	1.16	1.57	1.68
Lu	0.150	0.216	0.244	0.249	0.169	0.207	0.233
Hf	2.10	3.19	3.38	3.65	2.45	2.97	3.50
Th	0.721	0.898	1.06	1.02	0.757	0.877	1.07
U	0.219	0.238	0.294	0.278	0.210	0.231	0.292
W	0.131	0.238	0.214	0.246	0.148	0.247	0.236
La/Sm_N	1.46	1.43	1.47	1.51	1.51	1.42	1.61
Gd/Yb_N	2.33	2.29	2.35	2.31	2.23	2.17	2.38
Nb/Nb*	1.54	1.75	1.59	1.62	1.56	1.73	1.53
W/Th	0.182	0.265	0.202	0.242	0.196	0.281	0.220

Konchozero sill rocks														
Sample No.	**9112/1**	**9112/2**	**9701**	**689-7**	**9112/3**	**9702**	**9704**	***9705***	**689-1**	**689-2**	**689-3**	**689-4**	**689-5**	**689-6**
Cu	343	355	347	382	132	284	232	243	201	111	104	95.8	88.9	147
Sc	31.3	32.5	33.3	33.6	22.4	28.3	20.9	22.4	24.5	19.7	19.4	19.4	19.1	23.0
Y	22.1	22.5	23.6	24.6	7.74	19.7	7.41	7.88	13.3	7.88	7.83	8.38	7.22	7.72
Zr	135	140	142	147	44.3	124	45.2	44.7	83.6	46.3	46.8	50.5	39.9	44.0
Nb	15.0	15.3	15.8	16.6	5.46	13.9	5.59	6.07	10.3	5.87	5.68	6.14	5.18	5.27
La	10.8	11.2	12.1	12.8	4.60	10.3	4.58	4.78	7.60	4.91	4.75	4.85	4.32	4.54
Ce	27.2	27.0	29.3	31.0	10.3	27.2	10.3	10.1	15.9	10.7	11.1	11.1	10.0	10.6
Pr	4.21	4.35	4.67	4.96	1.44	4.19	1.41	1.53	2.50	1.56	1.51	1.57	1.38	1.46
Nd	17.9	17.7	18.7	19.7	6.88	17.8	6.61	7.14	12.0	7.25	7.14	7.90	6.45	6.91
Sm	4.58	4.54	4.99	5.14	1.80	4.60	1.74	1.85	3.14	1.86	1.83	1.93	1.66	1.80
Eu	1.49	1.52	1.60	1.88	0.594	1.61	0.598	0.623	1.08	0.621	0.619	0.643	0.543	0.596
Gd	4.74	4.90	5.12	5.42	1.96	4.68	1.96	2.07	3.27	2.02	1.95	2.01	1.77	1.93
Tb	0.842	0.854	0.884	0.879	0.289	0.725	0.285	0.303	0.493	0.300	0.296	0.310	0.269	0.293
Dy	4.48	4.54	4.66	4.81	1.72	4.15	1.68	1.76	2.92	1.75	1.73	1.77	1.56	1.71
Ho	0.822	0.837	0.860	0.915	0.315	0.773	0.309	0.336	0.549	0.326	0.319	0.339	0.295	0.320
Er	2.06	2.10	2.19	2.27	0.862	1.90	0.836	0.879	1.45	0.867	0.853	0.899	0.780	0.845
Tm	0.315	0.321	0.331	0.342	0.113	0.271	0.112	0.118	0.189	0.116	0.115	0.118	0.105	0.113
Yb	1.75	1.78	1.85	1.83	0.728	1.69	0.704	0.743	1.21	0.727	0.718	0.742	0.656	0.712
Lu	0.262	0.271	0.280	0.297	0.100	0.235	0.100	0.106	0.170	0.102	0.100	0.103	0.094	0.100
Hf	3.83	3.90	3.98	4.12	1.37	3.56	1.33	1.38	2.43	1.38	1.41	1.42	1.22	1.36
Th	1.02	1.03	1.12	1.13	0.336	0.957	0.314	0.350	0.629	0.352	0.352	0.392	0.318	0.337
U	0.277	0.270	0.299	0.302	0.0911	0.229	0.0876	0.0945	0.176	0.0968	0.0949	0.110	0.0927	0.0876
W	0.151	0.172	0.188	0.159	0.0778	0.164	0.0747	0.0833	0.121	0.0759	0.0565	0.0622	0.0534	0.0542
La/Sm_N	1.48	1.56	1.53	1.56	1.61	1.41	1.65	1.63	1.52	1.66	1.63	1.58	1.64	1.59
Gd/Yb_N	2.19	2.23	2.23	2.40	2.18	2.24	2.25	2.25	2.20	2.25	2.19	2.19	2.18	2.19
Nb/Nb*	1.64	1.62	1.55	1.58	1.59	1.60	1.69	1.70	1.70	1.61	1.59	1.61	1.60	1.54
W/Th	0.148	0.167	0.168	0.140	0.232	0.171	0.238	0.238	0.193	0.216	0.161	0.159	0.168	0.161

liquidus olivine in the pyroxene-olivine cumulates of 44.1 ± 0.5 wt% MgO. These authors calculated that such olivine would be in equilibrium with the emplaced picritic magma containing 8.0 ± 0.3 wt% MgO, in good agreement with the estimate by Puchtel et al. (1998). It is noteworthy that these estimates are significantly lower than the MgO content of the Angozero picrites, indicating that these picritic magmas contained excess cumulate olivine and clinopyroxene, as is also evident from their mineral compositions.

Shown in Fig. 5 are BSE-normalized lithophile trace element abundances in the Angozero picrites and the Konchozero sill rocks. The rocks are characterized by moderate enrichments in LREE, depletions in HREE ($La/Sm_N = 1.5 \pm 0.2$, $Gd/Yb_N = 2.2 \pm 0.1$), and positive Nb anomalies ($Nb/Nb^* = 1.6 \pm 0.1$). They also have low $Al_2O_3/TiO_2 = 6.0 \pm 1.1$ and high $Zr/Y = 6.0 \pm 0.5$ relative to the chondritic values of, respectively, 22.4 and 2.47, indicating relative depletions in Al, Y, and HREE.

4.2. $^{146,147}Sm$-$^{142,143}Nd$ and ^{176}Lu-^{176}Hf isotopic data

The ^{147}Sm-^{143}Nd and ^{176}Lu-^{176}Hf data are presented in Tables 3 and 4, respectively, and plotted on isochron diagrams in Fig. 6a,b. In the Sm-Nd isochron diagram (Fig. 6a), the Konchozero whole-rock and clinopyroxene mineral separate data from this study, combined with those from the study of Puchtel et al. (1998), define a regression line with a slope corresponding to an ISOPLOT Model 3 (MSWD = 2.9) age of 1977 ± 30 Ma and an average initial $\varepsilon^{143}Nd = +3.0 \pm 0.5$ (2SD). Including the data for the Angozero picrites from the Puchtel et al. (1998) study in the

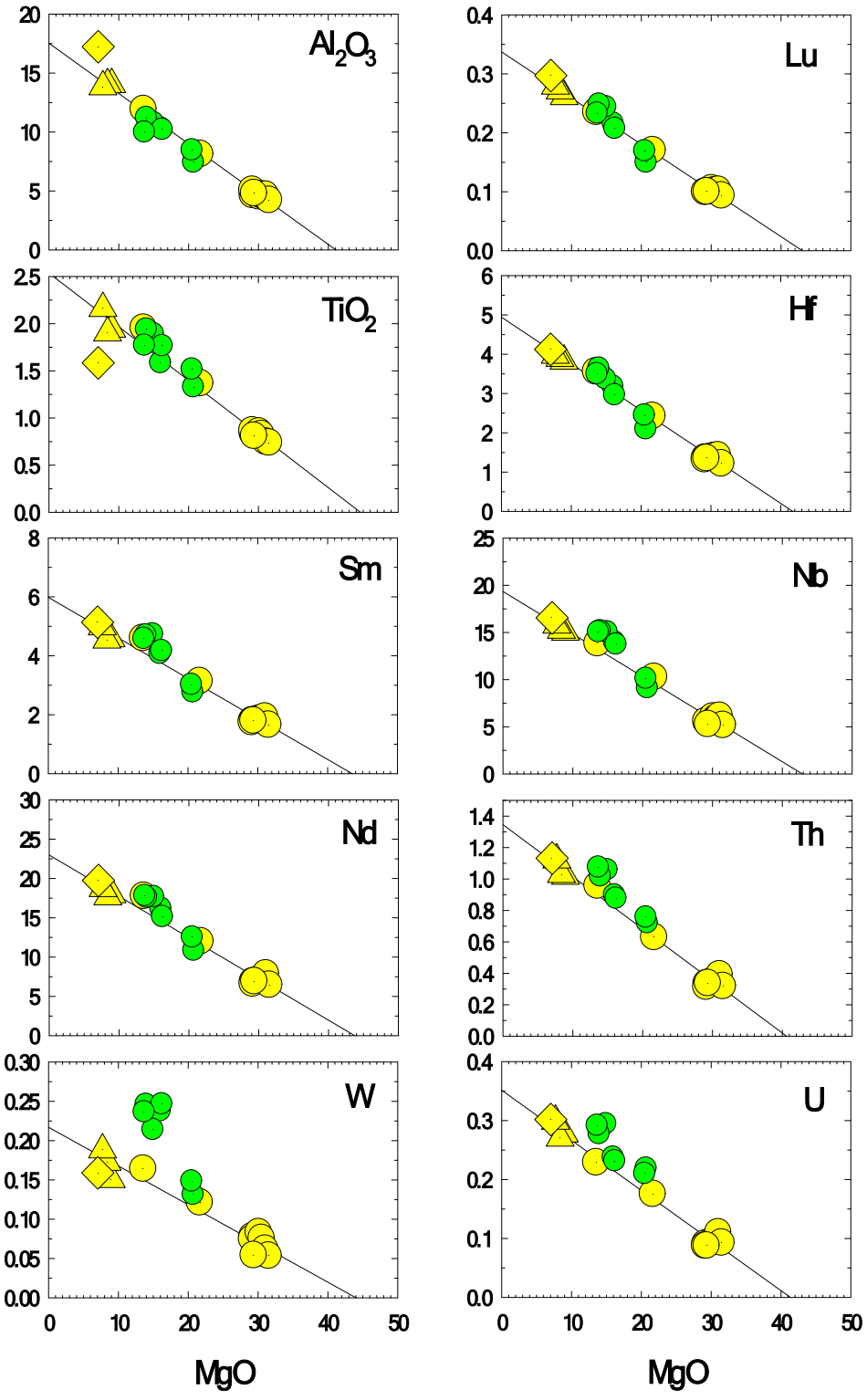

Fig. 4. Abundances of major (wt. %) and trace (ppm) elements plotted against the MgO contents in the Angozero picrites and the Konchozero sill rocks. The regression lines are drawn through the Konchozero data only. For legend see Fig. 5.

regression calculations yields a slightly less precise, but statistically identical, ISOPLOT Model 3 (MSWD = 3.4) age of 2005 ± 56 Ma and an average initial ε^{143}Nd = +2.9 ± 0.7 (2SD).

In the Lu-Hf isochron diagram (Fig. 6b), the Konchozero whole-rock and clinopyroxene mineral separate data define a regression line with a slope corresponding to an ISOPLOT Model 3 (MSWD = 7.2) age of 1990 ± 170 Ma and an average initial ε^{176}Hf = +2.8 ± 1.2 (2SD).

The ^{142}Nd data are presented in Table 5 and plotted in Fig. 7. The complete dataset for the high-precision Nd isotopic analyses can be found in Supplementary ***Table S5***. A total of six samples, including two Angozero picrites and four Konchozero sill rocks, were analyzed. The calculated average μ^{142}Nd of –1.1 ± 3.3 (2SD, *N* = 12) is

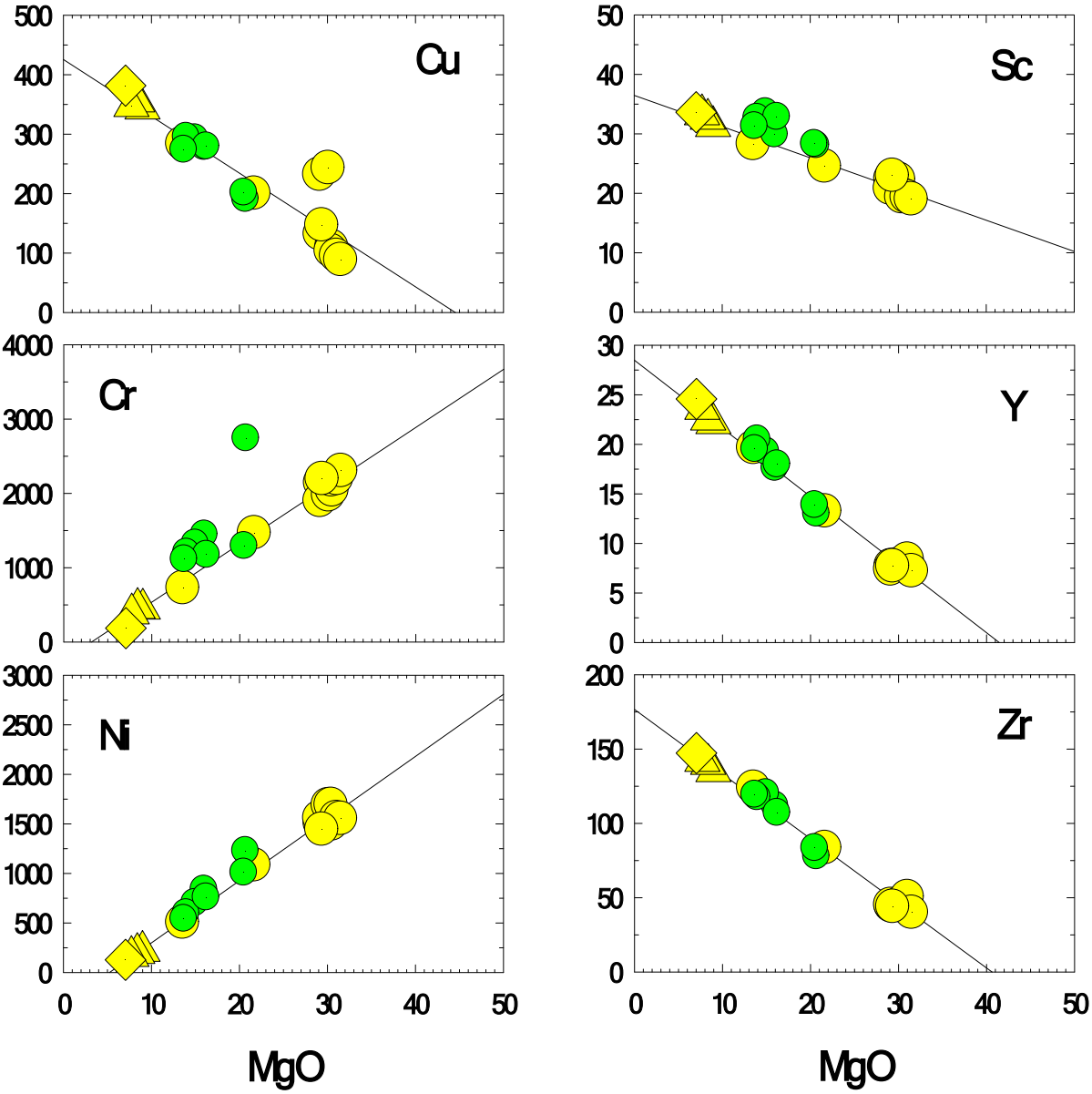

Fig. 4. (*continued*).

indistinguishable, within the uncertainty, from that of the JNdi Nd standard analyzed during the course of this analytical campaign (μ^{142}Nd = 0.0 ± 3.7, 2SD, N = 4).

4.3. ^{187}Re-^{187}Os and ^{190}Pt-^{186}Os isotopic and HSE abundance data

The HSE abundance data for the Angozero picrites and Konchozero sill rocks are presented in Table 6 and plotted on MgO versus HSE variation diagrams in Fig. 8, and as CI chondrite-normalized values in Fig. 9.

All HSE, except for Re, show broad positive correlations with the MgO content in both the picrites and the Konchozero sill rocks. Rhenium abundances, by contrast, plot with a considerable scatter and generally do not exhibit any meaningful correlations. In addition, the picrites show a substantially larger scatter in Pt and Pd abundances compared to the Konchozero sill rocks (Fig. 8).

The CI chondrite-normalized HSE abundance patterns in the Angozero picrites (Fig. 9) display variable Os/Ir_N = 0.71–1.6 and moderate enrichments in Pt and Pd over Os and Ir (Pd/Ir_N = 1.4–13) in all samples but one aliquot of 9108, which is enriched in Ir relative to Pd (Pd/Ir_N = 0.33). In the Konchozero sill rocks, the gabbro and the upper chilled margin samples show the largest degree of fractionation among the HSE (Os/Ir_N = 0.44–0.45, Pd/Ir_N = 23–24), whereas the olivine-pyroxene cumulates exhibit patterns similar to those of the picrites (Os/Ir_N = 0.77–1.4, Pd/Ir_N = 1.4–2.9). The two chromite separates from the Konchozero olivine-pyroxene cumulates show W-type patterns with elevated Os, Ir, Ru, and Re relative to the whole-rock samples.

The Re-Os isotopic data are listed in Table 6 and plotted on the Re-Os isochron diagram in Fig. 10. In the Re-Os isochron diagram, the whole-rock Konchozero sill samples and chromite separates yield an ISOPLOT Model 3 (MSWD = 78) age of 1974 ± 22 Ma and a slightly supra-chondritic initial γ^{187}Os = +2.9 ± 0.4 (Fig. 10a). Regression of the low-Re/Os (^{187}Re/^{188}Os < 2.5) samples, which include the olivine-pyroxene cumulates and chromite separates only, yields identical, albeit a less precise, age of 1968 ± 40 Ma and an initial γ^{187}Os = +2.9 ± 0.5 (Fig. 10b). The Angozero picrite samples, on the other hand, plot with a large scatter to the left of the regression line (Fig. 10b), likely due to the loss of Re from these rocks during alteration that occurred a few hundred Ma after lava emplacement.

The Pt-Os isotopic data are presented in Table 7 and plotted on the

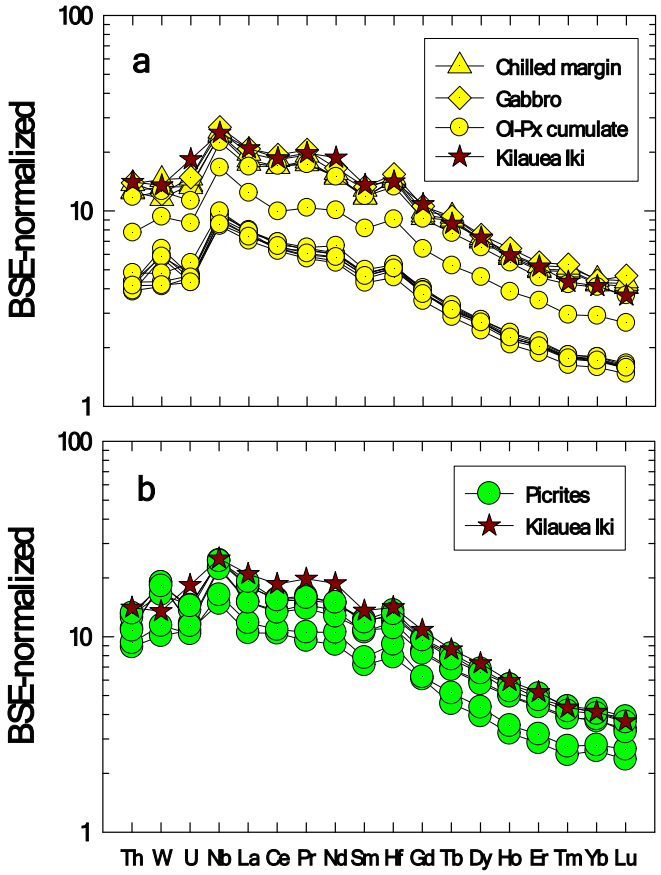

Fig. 5. Abundances of selected trace elements normalized to the BSE values of Hofmann (1988) in the Angozero picrites and the Konchozero sill rocks. The data for an average Kilauea Iki lava lake picrite obtained in this study are plotted for comparison.

Pt-Os isochron diagram in Fig. 11. The two Konchozero whole-rock olivine-pyroxene cumulates and three chromite separates define an isochron with a slope corresponding to an age of 2010 ± 402 Ma, consistent with the emplacement age of the Suisarian suite. The calculated average initial $\mu^{186}Os = +4.9 \pm 2.1$ is near-chondritic, implying that the mantle source of these rocks evolved with a long-term near-chondritic Pt/Os ratio.

4.4. Tungsten isotope and abundance data

The W abundances in the Angozero picrites and Konchozero sill rocks are listed in Table 2 and plotted as a function of MgO content in Fig. 4. In the Angozero picrites, the W abundances vary between 0.13 and 0.25 ppm, and in the Konchozero sill rocks – between 0.053 and 0.19 ppm. The W abundance data for the Konchozero sill rocks plot along the liquid line of descent in Fig. 4, indicating magmatic behavior of W, which is also supported by the BSE-like W/Th ratios in these rocks averaging 0.18 ± 0.07 (2SD). The Angozero picrites, on the other hand, have somewhat higher relative W abundances at a given MgO content and plot along a steeper trend relative to the Konchozero sill rocks. The W/Th ratios in the Angozero picrites are also somewhat higher, averaging 0.23 ± 0.07 (2SD), although both ratios are identical within their respective uncertainties and the average value of 0.20 ± 0.08 is similar to the BSE estimate of 0.19 (McDonough and Sun, 1995).

The ^{182}W data for the Angozero picrites and Konchozero sill rocks are listed in Table 8 and plotted in Fig. 12. The complete dataset for the high-precision W isotopic analyses can be found in Supplementary ***Table S6***. The data obtained by the N-TIMS and MC ICP-MS techniques are identical within their respective uncertainties. The average $\mu^{182}W$ value for all the data of 0.0 ± 4.8 (2SD) indicates a modern BSE-like W isotopic composition of the Onega Basin source.

Table 3
Sm-Nd isotopic compositions and Sm and Nd abundances of the Angozero picrites and Konchozero sill rocks and clinopyroxene separates.

Sample	Sm, ppm	Nd, ppm	$^{147}Sm/^{144}Nd$	$^{143}Nd/^{144}Nd$	$\varepsilon^{143}Nd$ (*T*)
Konchozero sill rocks and Angozero picrites: Puchtel et al. (1998)					
9701	5.281	19.86	0.1611 ± 8	0.512322 ± 6	+2.9
9702	5.334	20.73	0.1559 ± 8	0.512235 ± 6	+2.5
9704	2.125	8.238	0.1559 ± 8	0.512275 ± 7	+3.3
9705	1.834	7.021	0.1579 ± 8	0.512283 ± 5	+2.9
9111	1.661	6.446	0.1557 ± 8	0.512272 ± 13	+3.3
9112	1.657	6.411	0.1563 ± 8	0.512271 ± 10	+3.1
9112/1	4.356	17.07	0.1543 ± 8	0.512247 ± 7	+3.2
9112/2	4.232	16.71	0.1531 ± 8	0.512240 ± 11	+3.3
9112/3	1.700	6.604	0.1556 ± 8	0.512255 ± 13	+3.0
9111 Cpx	1.809	4.886	0.2239 ± 11	0.513151 ± 14	+3.1
9112 Cpx	2.017	5.418	0.2251 ± 11	0.513159 ± 18	+3.0
9112/2 Cpx	2.127	6.007	0.2140 ± 11	0.513036 ± 9	+3.4
9112/3 Cpx	2.015	5.451	0.2234 ± 11	0.513149 ± 12	+3.2
89103	2.670	10.05	0.1605 ± 8	0.512269 ± 6	+2.1
89104	3.687	14.05	0.1587 ± 8	0.512295 ± 7	+3.1
89105	4.862	18.81	0.1563 ± 8	0.512255 ± 5	+2.9
89105/1	4.868	18.48	0.1593 ± 8	0.512267 ± 5	+2.4
Konchozero sill rocks: this study					
689-3	1.730	6.694	0.1562 ± 3	0.512265 ± 3	+3.0
689-4	1.823	7.215	0.1527 ± 3	0.512205 ± 3	+2.7
689-5	1.538	5.944	0.1564 ± 3	0.512253 ± 3	+2.7
689-3 Cpx	2.449	7.313	0.2025 ± 4	0.512859 ± 4	+2.8
689-4 Cpx	1.703	5.077	0.2028 ± 4	0.512869 ± 4	+3.0
689-5 Cpx	1.681	4.505	0.2255 ± 5	0.513152 ± 3	+2.7

The initial $\varepsilon^{143}Nd$ values were calculated for the emplacement age $T = 1977$ Ma defined by the Sm-Nd isochron.

Table 4
Lu-Hf isotopic compositions and Lu and Hf abundances of the Konchozero sill rocks and clinopyroxene separates.

Sample	Lu, ppm	Hf, ppm	$^{176}Lu/^{177}Hf$	$^{176}Hf/^{177}Hf$	$\varepsilon^{176}Hf$ (*T*)
9112/3	0.09796	1.235	0.01126 ± 2	0.282031 ± 15	+3.0
9702	0.2376	3.275	0.01030 ± 2	0.281995 ± 7	+3.1
9704	0.09481	1.158	0.01162 ± 2	0.282028 ± 4	+2.5
9705	0.09760	1.205	0.01149 ± 2	0.282031 ± 4	+2.7
9112/3 Cpx	0.1232	0.8779	0.01992 ± 4	0.282350 ± 6	+2.8
9704 Cpx	0.1022	0.7133	0.02035 ± 4	0.282348 ± 6	+2.2
9705 Cpx	0.1071	0.7319	0.02076 ± 4	0.282409 ± 13	+3.8

The initial $\varepsilon^{176}Hf$ values were calculated for the emplacement age $T = 1977$ Ma defined by the Sm-Nd isochron.

5. Discussion

5.1. Effects of secondary alteration

The Angozero picrites and Konchozero sill rocks were subjected to a relatively low degree of secondary alteration and it has been concluded that the major and trace element variations in these rocks define magmatic trends that are consistent with the primary mineralogy, except for the alkalis, CaO, SiO_2, Rb, Sr, and Ba (Puchtel et al., 1998). In agreement with this conclusion, the petrogenetically and geochronologically important lithophile trace elements Nd, Sm, Lu, and Hf plot along magmatic differentiation trends in diagrams of MgO versus trace element abundances (Fig. 4), indicating immobile behavior of these elements during secondary alteration processes.

This conclusion is also extended for all the HSE, except for Re in the picrites (Fig. 8), which apparently was mobilized during postmagmatic

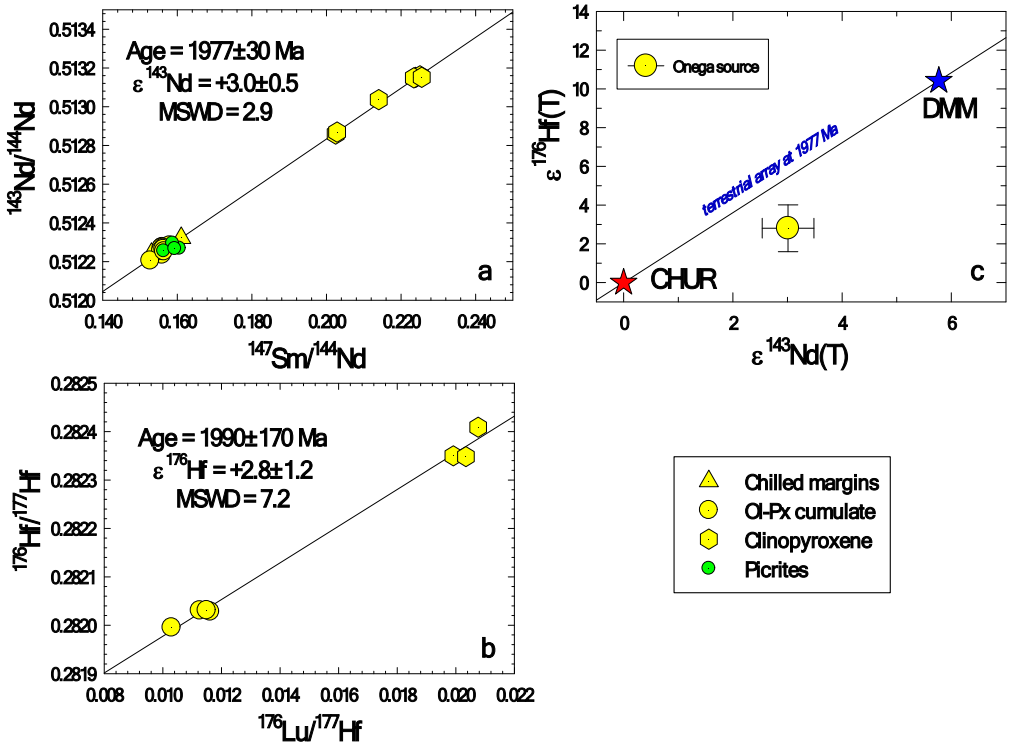

Fig. 6. (a) Combined Sm-Nd isochron for the Angozero picrites and Konchozero sill rocks using data from Puchtel et al. (1998) and this study. (b) Lu-Hf isochron for the Konchozero sill rocks. (c) Initial ε^{143}Nd versus initial ε^{176}Hf diagram for the Konchozero sill rocks. Note that the Onega Basin data point plots well below the terrestrial Nd-Hf mantle array at 1977 Ma.

Table 5
^{142}Nd data for the Angozero picrites, Konchozero sill rocks, and JNdi Nd standard.

	^{142}Nd/^{144}Nd	±2SE	μ^{142}Nd	±2SE
Samples				
89104_1	1.141835	0.000004	+1.2	3.6
89104_2	1.141835	0.000004	+1.5	3.2
89105_1	1.141829	0.000004	−4.0	3.6
89105_2	1.141832	0.000004	−1.3	3.1
9701_1	1.141833	0.000004	−0.2	3.3
9701_2	1.141834	0.000004	+0.2	3.1
9702_1	1.141830	0.000004	−2.8	3.2
9702_2	1.141831	0.000004	−1.7	3.6
9704_1	1.141832	0.000004	−1.4	3.5
9704_2	1.141832	0.000004	−0.9	3.6
9705_1	1.141832	0.000004	−1.0	3.1
9705_2	1.141830	0.000004	−2.8	3.4
Average (±2SD)	**1.141832**	**0.000004**	**−1.1**	**3.3**
JNdi Nd standard				
F02_JNdi 600 ng	1.141833	0.000003	+0.2	2.6
F03_JNdi 600 ng	1.141835	0.000004	+1.8	3.1
F04_JNdi 600 ng	1.141830	0.000003	−2.5	3.0
F05_JNdi 600 ng	1.141834	0.000004	+0.5	3.8
Average (±2SD)	**1.141833**	**0.000004**	**0.0**	**3.7**

The complete isotope dataset is presented in the Supplementary Table S5.

processes several hundred million years after lava emplacement, as evidenced by a large scatter of the Re abundance data on the Re versus MgO diagram (Fig. 8) and Re-Os isotopic data on the Re-Os isochron diagram (Fig. 10). On the other hand, Re mobility in the Konchozero sill rocks was limited. The Re-Os isochron age obtained here for the Konchozero sill rocks is consistent with the Sm-Nd and U-Pb ages for the entire suite of samples (Puchtel et al., 1998, 1999; this study), impying that the Re-Os system remained closed in the Konchozero sill since its emplacement.

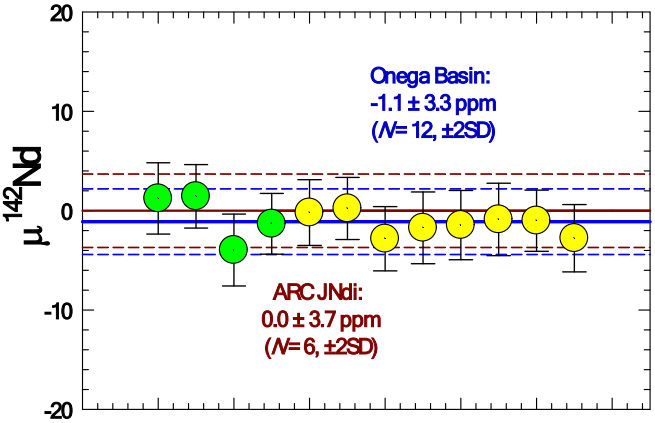

Fig. 7. ^{142}Nd compositions of the Angozero picrite and Konchozero sill samples analyzed in this study. The data are reported in μ^{142}Nd units, which are the part per million (ppm) deviation of the ^{142}Nd/^{144}Nd ratio in a given sample relative to the mean ^{142}Nd/^{144}Nd ratio measured for the JNdi Nd standard. The external precision of the standard measurements during the present analytical campaign was 3.7 ppm. Each sample load was run twice and the data were averaged.

Collectively, the majority of lithophile and siderophile trace element and isotope systematics of the Angozero picrites and Konchozero sill rocks have remained mostly unaffected by alteration and reflect those of their mantle source region. The nature of the processes that controlled the geochemical and isotope features of that source will be discussed in the following sections.

5.2. *Composition and generation of the emplaced picritic magmas*

The geochemical similarities and close spatial association (Figs. 4, 5) of the Angozero picrites and the Konchozero sill rocks indicate that they

Table 6
HSE abundances (in ppb) and Re-Os isotopic data for the Angozero picrites and Konchozero sill rocks.

Sample No.	Re	Os	Ir	Ru	Pt	Pd	$^{187}Re/^{188}Os$	$^{187}Os/^{188}Os$	$\gamma^{187}Os(T)$
9701	1.007	0.0797	0.1657	0.3966	3.379	2.122	82.76 ± 1.23	2.8858 ± 0.0049	+4.7
9702	0.2439	0.4720	0.5918	1.669	4.203	2.101	2.514 ± 0.009	0.20031 ± 0.00051	+2.3
Replicate	0.2384	1.017	0.8762	1.712	4.151	2.018	1.134 ± 0.005	0.15548 ± 0.00008	+3.5
9704	0.4059	2.876	2.379	5.182	10.05	7.216	0.6809 ± 0.0019	0.13824 ± 0.00010	+1.7
Replicate	0.4155	3.370	2.461	6.261	10.52	7.013	0.5948 ± 0.0015	0.13558 ± 0.00012	+1.9
9705	0.4804	3.642	2.993	5.288	9.813	7.293	0.6363 ± 0.0016	0.13770 ± 0.00010	+2.5
Replicate	0.4670	3.448	2.611	4.888	9.683	7.517	0.6537 ± 0.0016	0.13844 ± 0.00013	+2.6
9112/3	0.4517	4.777	3.262	5.452	9.821	7.128	0.4537 ± 0.0012	0.13103 ± 0.00012	+2.0
Replicate	0.3983	3.340	2.638	5.145	9.975	6.716	0.5753 ± 0.0017	0.13577 ± 0.00012	+2.6
689-1	0.5312	1.481	1.528	3.910	8.241	3.199	1.739 ± 0.004	0.17494 ± 0.00006	+2.8
689-3	0.5535	3.445	2.688	3.572	10.50	7.918	0.7757 ± 0.0019	0.14294 ± 0.00004	+3.0
689-4	0.5052	3.746	2.824	4.653	8.004	5.863	0.6509 ± 0.0017	0.14024 ± 0.00004	+4.3
689-5	0.2943	4.040	3.040	5.535	8.776	5.490	0.3507 ± 0.0014	0.12926 ± 0.00006	+3.5
689-6	0.3273	2.621	2.131	3.415	11.60	7.911	0.6019 ± 0.0023	0.13711 ± 0.00006	+3.0
689-7	0.3871	0.02073	0.04543	0.1077	3.917	1.413	147.3 ± 3.9	5.0505 ± 0.0039	+11
89103	0.0923	1.833	1.538	4.037	8.234	25.40	0.2430 ± 0.0023	0.14062 ± 0.00007	+17
89104	0.1225	0.9069	1.026	2.761	6.650	5.968	0.6582 ± 0.0045	0.21196 ± 0.00011	+67
89105	0.1695	0.7832	0.8771	2.817	4.452	2.274	1.065 ± 0.006	0.28978 ± 0.00017	+124
89105/1	0.2296	0.7691	0.8944	2.255	7.921	5.189	1.468 ± 0.006	0.28555 ± 0.00016	+108
9108	0.1310	10.37	6.231	4.123	4.559	2.636	0.06088 ± 0.00055	0.12467 ± 0.00009	+8.0
Replicate	0.1311	1.365	1.199	3.040	4.427	2.706	0.4659 ± 0.0034	0.17336 ± 0.00009	+39
9109	0.1757	0.6416	0.8806	2.613	3.357	1.550	1.335 ± 0.007	0.21965 ± 0.00011	+54
9109/1	0.1654	0.5687	0.6903	1.952	13.23	8.264	1.425 ± 0.008	0.25673 ± 0.00016	+84
9704 Chr	3.183	21.52	12.87	35.06	22.97	7.499	0.7140 ± 0.0042	0.14127 ± 0.00014	+3.4
9705 Chr	8.875	33.35	26.39	89.71	56.01	25.28	1.288 ± 0.006	0.15957 ± 0.00014	+2.6
689-3 Chr	2.290	25.12					0.4395 ± 0.0031	0.13063 ± 0.00006	+2.1
689-4 Chr	2.636	18.81					0.6763 ± 0.0043	0.13899 ± 0.00008	+2.5
689-5 Chr	2.085	12.90					0.7803 ± 0.0026	0.14359 ± 0.00007	+3.5
689-6 Chr	2.141	37.76					0.2732 ± 0.0018	0.12648 ± 0.00006	+3.3
9704_1-12*	0.3828	2.911	2.255		9.584		0.6378 ± 0.0043	0.13691 ± 0.00011	+1.8
9705_1-12*	0.4388	3.284	2.596		9.030		0.6450 ± 0.0039	0.13807 ± 0.00012	+2.6
689-4 Chr1_1-4*	1.956	7.534	5.146		16.56		1.256 ± 0.0094	0.15900 ± 0.00008	+3.0
689-4 Chr1_5-8*	1.833	8.905	6.300		13.64		0.9949 ± 0.0083	0.15126 ± 0.00007	+3.9
689-4 Chr2_1-4*	1.162	11.57	8.854		26.19		0.4843 ± 0.0059	0.13357 ± 0.00006	+3.3
689-4 Chr2_5-8*	1.335	16.24	12.69		48.18		0.3964 ± 0.0043	0.13113 ± 0.00005	+3.8
689-4 Chr1+2_1-4*	1.638	11.44	8.183		20.02		0.6912 ± 0.0063	0.14033 ± 0.00009	+3.2
689-4 Chr1+2_5-8*	2.184	18.75	12.49		25.97		0.5618 ± 0.0040	0.13570 ± 0.00007	+2.9

*Spiked aliquots of subsamples from the unspiked digestions used to determine the Pt/Os and Re/Os ratios. The HSE abundances were recalculated on an anhydrous basis using the LOI values from Table 1. Initial $\gamma^{187}Os$ values were calculated at $T = 1974$ Ma defined by the Re-Os isochron using the parameters specified in the text. *Replicate* – replicate digestions of the same samples.

were linked to a single volcano-plutonic center (Puchtel et al., 1998). Their chemical features are used here to provide constraints on the composition and the conditions of generation of the emplaced magmas. It is inferred that the emplaced magmas contained between 8 and 10 wt % MgO on the basis of the composition of the chilled margin samples 9112/1–12/2 from the Konchozero sill and the intersection values of the incompatible trace element trends with the MgO axes (Puchtel et al., 1998). This estimate has been confirmed by the study of newly found primary liquidus olivine phenocrysts in the Konchozero sill pyroxene-olivine cumulate rocks by Nicklas et al. (2019), who estimated that the emplaced magma contained 8.0 ± 0.3 wt% MgO. Puchtel et al. (1998) noted, however, that, as is the case with other mantle plume-generated flood basalt provinces, this estimate likely does not represent the composition of the parental magma, but rather the composition of an evolved liquid that resulted from differentiation of the parental picritic magma containing 14–15 wt% MgO. These authors also emphasized that the Al-depleted nature of the rocks required generation of the parental melt in the garnet stability field, at depths >100 km. The parental picritic magmas must have separated from their source region while still in the garnet stability field, as evidenced by the lack of variation in the degree of Al depletion across the entire Onega Basin sample set.

Upon separation from the mantle plume source, the parental picritic magmas must have passed through the subcontinental lithospheric mantle and continental crust *en route* to the surface and have undergone magmatic differentiation. As evident from the petrography and chemistry of the picrites and the Konchozero sill rocks (Figs. 4 and 5), this differentiation was controlled by two major liquidus phases, olivine and clinopyroxene. A minor liquidus phase included chromite, and its fractionation, along with olivine and clinopyroxene, is manifested by the positive correlation in the MgO versus Cr diagram (Fig. 5). This liquidus mineral assemblage is consistent with the experimental data indicating that at 1 atm, clinopyroxene starts crystallizing from a liquid containing ~8.5 % MgO (Kinzler and Grove, 1985), and increasing pressure extends the pyroxene stability field towards more MgO-rich compositions (Elthon and Scarfe, 1984). The parental picritic magmas with 14–15 wt % MgO likely differentiated in sub-crustal magma chambers and then the evolved olivine + pyroxene mush erupted either as thin picritic flows, which solidified before any substantial differentiation occurred, or were emplaced as shallow-level sills, such as the Konchozero sill, which represented larger and, thus, more strongly differentiated bodies.

5.3. *Effects of crustal contamination and composition of the mantle source*

The Angozero picrites and Konchozero sill rocks are significantly enriched in Nb relative to Th and La and, as a result, exhibit uniform, large positive Nb anomalies ($Nb/Nb^* = 1.6 \pm 0.1$, where $Nb/Nb^* = Nb_N/\sqrt{[Th_N{*}La_N]}$), indicating that their parental magma did not experience any significant degree of crustal contamination. This is because upper crustal rocks are generally characterized by low Nb/Th_N and Nb/La_N ratios and, thus, exhibit pronounced negative Nb/Nb* anomalies compared to the BSE (e.g., Rudnick and Gao, 2003; 2014). Because of much lower Th, Nb, and La abundances in primary mafic–ultramafic

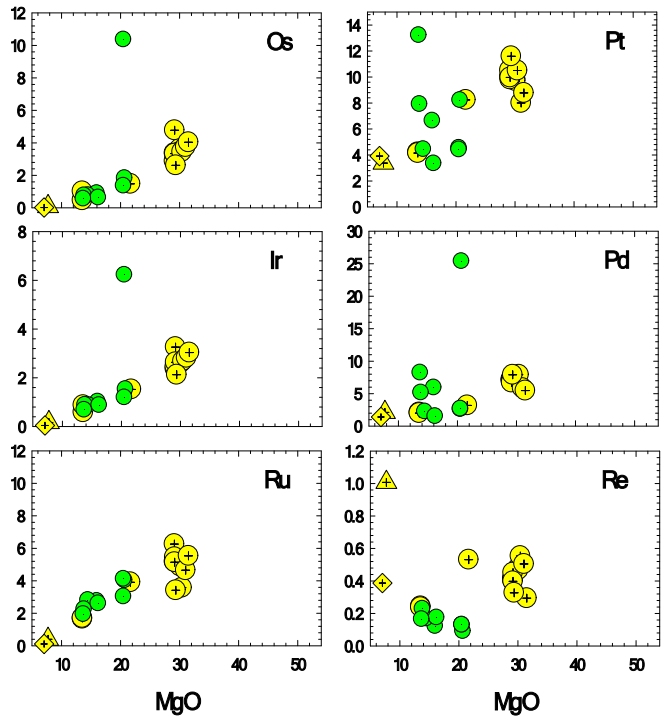

Fig. 8. Abundances of HSE (in ppb) plotted against MgO content (in wt. %) in the Angozero picrites and Konchozero sill rocks. For legend see Fig. 9.

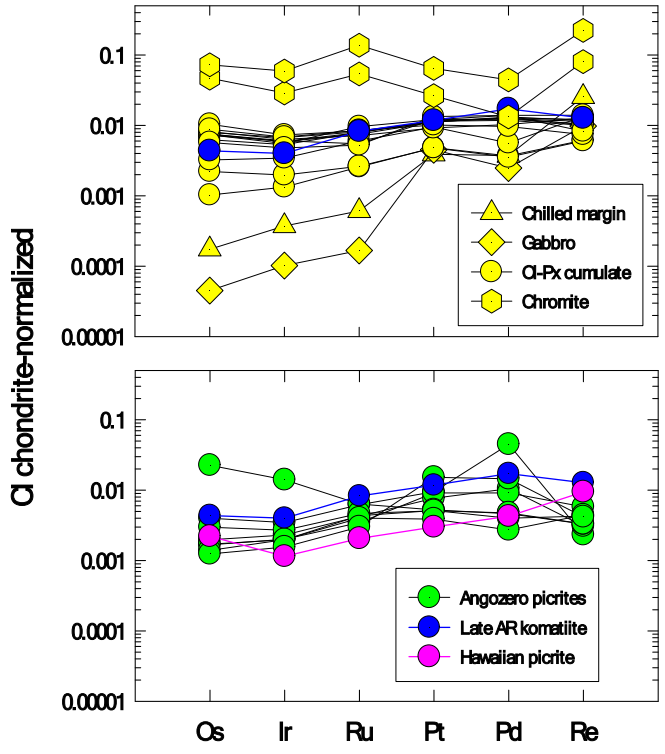

Fig. 9. CI chondrite-normalized (normalizing values from Horan et al., 2003) HSE abundances in the Angozero picrites, Konchozero sill rocks, and chromite separates.

magmas, which commonly have Nb/Nb* ≥ 1.0, crustal contamination usually results in variably negative Nb/Nb* anomalies in these magmas (e.g., Jochum et al., 1991).

The Angozero picrites and Konchozero sill rocks are enriched in

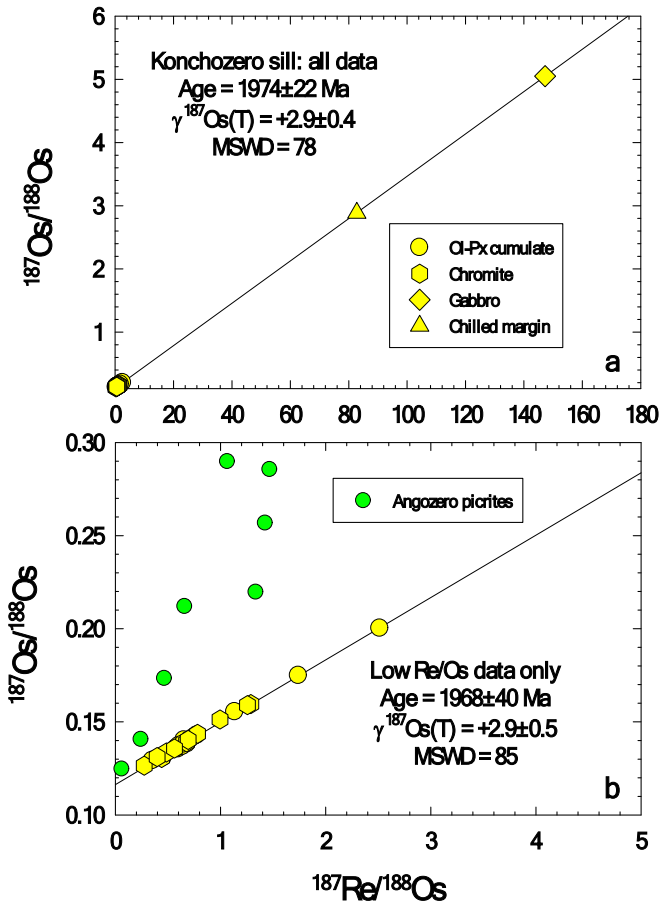

Fig. 10. Re-Os isochron diagrams for all Konchozero sill samples and chromite separates **(a)** and for low-Re/Os Konchozero olivine-pyroxene cumulates and chromite separates only **(b)** Also plotted in **(b)** are data for the Angozero picrites which were not included in the isochron calculations.

LREE and other highly incompatible lithophile trace elements ($La/Sm_N = 1.5 \pm 0.2$). At the same time, the rocks have a positive initial $\varepsilon^{143}Nd$ value of $+ 3.0 \pm 0.5$, implying derivation from a long-term LREE-depleted mantle source that must have evolved with a minimum time-integrated suprachondritic $^{147}Sm/^{144}Nd$ ratio of 0.2054 ± 0.0014 versus 0.1967 in CHUR. The observed LREE-enrichment of the picritic magmas could be a feature of either the original source or the magma generation process, or a combination of both. In either case, the LREE-enrichment must have occurred within a short time interval of the melting event that produced the magmas to satisfy the LREE-depletion requirement imposed by the Nd isotopic data.

As discussed in the previous section, the Onega Basin picritic magmas must have been generated in the garnet peridotite stability field, in equilibrium with garnet in the melting residue. Our model calculations show that the trace element pattern of the parental picritic magma with ~14 wt% MgO, represented by, e.g., sample 89105/1, can be reproduced by 3 % batch melting of a LREE-depleted ($La/Sm_N = 0.68$, $^{147}Sm/^{144}Nd = 0.2337$) garnet lherzolite source composed of 68 % Ol, 20 % Opx, 10 % Cpx and 2.0 % garnet and using the partition coefficients of Green (1994). This composition of the source is rather restrictive and it requires a relatively low modal abundance of garnet in the source of 2 %, whereas typical garnet lherzolite contains 5–10 % garnet. It also requires the source to be more strongly depleted in LREE than is estimated from the ^{147}Sm-^{143}Nd systematics ($^{147}Sm/^{144}Nd = 0.2337$ versus 0.2054). Even a small increase in the abundance of garnet in the source would require a HREE-enriched and an even more LREE-depleted source to match the composition of the Onega Basin parental magmas. For example, a source with 3 % garnet would require Yb

Table 7
High-precision ^{186,187}Os data for the Konchozero sill rocks and chromite separates.

Sample No.	^{190}Pt/^{188}Os	^{184}Os/^{188}Os	^{186}Os/^{188}Os	^{187}Os/^{188}Os	μ^{186}Os(*T*)
9704	0.003159 ± 16	0.0013065 ± 19	0.1198435 ± 11	0.136957 ± 3	+6.1 ± 8.8
9705	0.002628 ± 13	0.0013030 ± 17	0.1198417 ± 12	0.138070 ± 5	+3.4 ± 10
689-4 Chr1	0.001791 ± 9	0.0013041 ± 6	0.1198394 ± 8	0.1557899 ± 9	+4.4 ± 6.6
689-4 Chr2	0.002506 ± 13	0.0013052 ± 5	0.1198416 ± 7	0.1324293 ± 5	+5.7 ± 5.9
689-4 Chr1 + 2	0.001497 ± 7	0.0013051 ± 4	0.1198386 ± 6	0.1379326 ± 6	+5.0 ± 4.9
Average (±2SD)					**+4.9 ± 2.1**

The initial μ^{186}Os values were calculated at $T = 1974$ Ma defined by the Re-Os isochron using the parameters specified in the text.

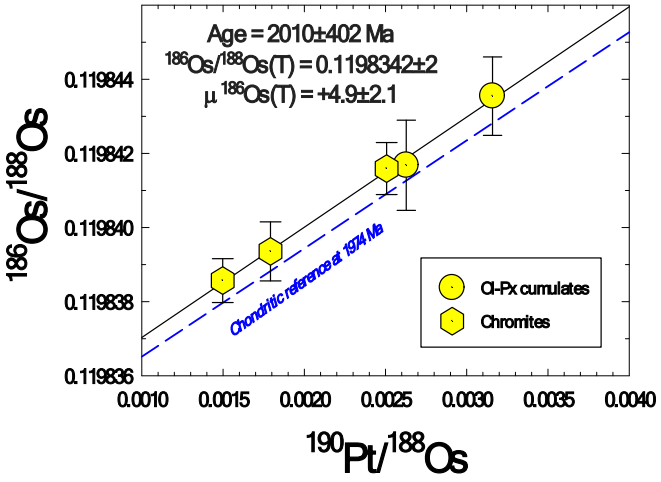

Fig. 11. Pt-Os isochron diagram for the Konchozero sill olivine-pyroxene cumulate samples and chromite separates.

Table 8
Tungsten isotopic compositions and W/Th ratios in the Angozero picrites and Konchozero sill rocks.

Sample No.	Lithology	μ^{182}W	μ^{183}W	W/Th
N-TIMS data				
689-1*	Ol-Px cumulate	–1.6 ± 5.4	+2.8 ± 3.8	0.193
689-6*	Ol-Px cumulate	–2.2 ± 3.4	+2.8 ± 2.7	0.161
689-7*	Gabbro	+5.2 ± 5.3	–3.7 ± 3.9	0.140
89105*	Picrite	–4.3 ± 3.3	+0.9 ± 2.8	0.202
9109/1**	Picrite	+0.7 ± 3.0	+4.8 ± 2.3	0.220
Replicate**	Picrite	–2.5 ± 2.7	+4.5 ± 2.0	0.220
MC ICP-MS data				
689-7*	Gabbro	+1.1 ± 4.1	–4.0 ± 3.4	0.140
Replicate*	Gabbro	+0.44 ± 2.9	–3.8 ± 3.1	0.140
89105*	Picrite	+0.34 ± 3.5	–5.4 ± 4.3	0.202
Replicate*	Picrite	+1.0 ± 4.3	–3.1 ± 3.9	0.202
89105/1*	Picrite	+0.68 ± 4.2	+0.1 ± 3.1	0.242
Replicate*	Picrite	+1.1 ± 3.2	–1.8 ± 2.8	0.242
Average (±2SD)		**+0.01 ± 4.8**		

The $\mu^{182,183}W = [(^{182,183}W/^{184}W)_{sample}/(^{182,183}W/^{184}W)_{standard} - 1] \times 10^6$ are normalized to $^{186}W/^{183}W = 1.98590$ (N-TIMS) or $^{186}W/^{184}W = 0.92767$ (MC-ICP-MS). Note that the μ^{183}W values obtained by MC-ICP-MS are subject to the analytical ^{183}W effect (Budde et al., 2022), resulting in small negative anomalies (see section 3.5 for details). Uncertainties on the W isotopic compositions obtained by N-TIMS are the 2SE in-run precision for individual analyses. Uncertainties of the W isotopic compositions obtained by MC-ICP-MS represent the 95 % confidence intervals of solution replicates (N = 9–11).
Ol-Px cumulate – olivine-pyroxene cumulate from the Konchozero sill. Replicate – replicate digestions of the same sample. *Processed and analyzed at the *IGL/PL*. **Processed and analyzed at the *IGGRC*. The additional details are provided in the Analaytical Techniques section; the complete dataset is presented in the Supplementary Table S6.

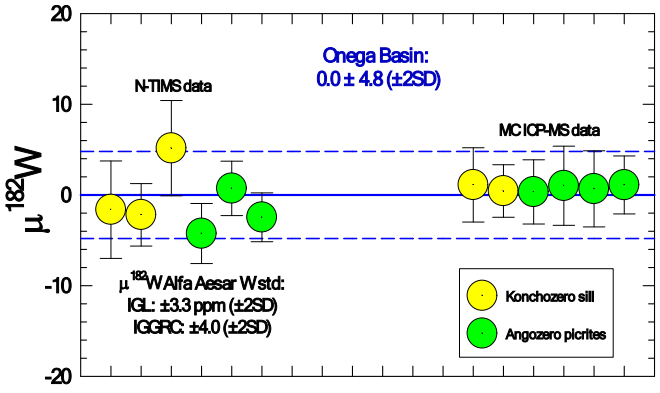

Fig. 12. Tungsten isotopic data for the Angozero picrites and Konchozero sill rocks obtained by N-TIMS and MC ICP-MS.

abundances in the source to be ~34 % higher ($Gd/Yb_N = 0.818$) relative to the BSE, and a $^{147}Sm/^{144}Nd = 0.2431$. Such a LREE-depletion, accompanied by the HREE-enrichment, may have resulted from addition of a recycled basaltic crust to a BSE-like source of the Onega Basin picritic magmas, as has been proposed to explain the genesis of a variety of OIB by a number of authors (e.g., Hofmann and White, 1982; White and Hofmann, 1982; White, 1985; Hofmann, 1988; Hofmann and Jochum, 1996; Kogiso et al., 1998; Lassiter and Hauri, 1998; Norman and Garcia, 1999; Sobolev et al., 2007).

Oceanic island basalts containing a significant amount of subducted oceanic crust are also characterized by positive Hf/Hf* and Nb/Nb*anomalies (e.g., Willbold and Stracke, 2006), chemical features evident in the BSE-normalized patterns of both the Angozero and Kilauea picrites (Fig. 5), the latter having been argued to contain a significant proportion of subducted oceanic crust in their source (e.g., Lassiter and Hauri, 1998; Norman and Garcia, 1999; Sobolev et al., 2005; Bizimis et al., 2007; Ren et al., 2009; Pietruszka et al., 2013). This is due to the fact that during the dehydration reactions that accompany subduction of oceanic lithosphere to form eclogite, the residual mineral assemblage normally would include rutile, a major host of HFSE (Stalder et al., 1998; Foley et al., 2000; Rudnick et al., 2000). As a result, an eclogitic slab will be characterized by positive Nb and Hf anomalies that will be transferred to the mantle source containing subducted, dehydrated oceanic crust, which usually contains a significant proportion of an oceanic gabbro component. This would also explain the strong depletion in Th relative to Nb (e.g., low Th/Nb ratios) and highly positive Nb/Nb* ratios observed in both the Onega Basin and Kilauea picrites (e.g., Hofmann and Jochum, 1996; Dale et al., 2007). In the following sections, we consider the impact of such recycled oceanic crust on the Nd, Hf, and Os isotopic systematics.

5.4. The origin of the decoupled Nd-Hf systematics

Generally, the terrestrial Nd-Hf mantle array originates from the coupled behavior of Nd and Hf isotopes in most terrestrial rocks, arising from the similar partitioning of the parent (Sm, Lu) and daughter (Nd,

Hf) elements of the ^{147}Sm-^{143}Nd and ^{176}Lu-^{176}Hf isotope systems during upper mantle melting and differentiation processes (e.g., Patchett et al., 1981; Salters and White, 1998; Vervoort and Blichert-Toft, 1999; Vervoort et al., 1999, 2000). The average initial ε^{176}Hf value for the Angozero picrites and Konchozero sill rocks, however, plots significantly below the Nd-Hf terrestrial mantle array in Fig. 6c, indicating a decoupled behavior of the two long-lived lithophile element isotope systems.

Certain conditions may account for a decoupled behavior of these isotope systems. Proposed mechanisms include the effects of early magma ocean crystallization (e.g., Caro et al., 2005; Rizo et al., 2011; Puchtel et al., 2013; 2016b; Hyung et al., 2016; Morino et al., 2017, 2018; Boyet et al., 2021), recycling and long-term storage of Hadean proto-crust (Tusch et al., 2022), magma mixing (Tappe et al., 2011; 2020b), post-emplacement disturbance of one or both isotope systems (Blichert-Toft et al., 2015), and recycling and long-term storage of oceanic crust and/or sediments in the mantle (Patchett et al., 1984; Blichert-Toft et al., 1999; Gaffney et al., 2007; Blichert-Toft et al., 2015).

Periodic magma oceans were likely a direct consequence of collisional planetary growth (e.g., Tonks and Melosh, 1993; Bottke et al., 2010; Rubie et al., 2011; Marchi et al., 2018). Crystallization of a magma ocean may have resulted in stratification controlled by fractionation of certain mineral assemblages, the compositions of which depend on the depth of the magma ocean (Elkins-Tanton et al., 2003; Caro et al., 2005; Labrosse et al., 2007; Elkins-Tanton, 2012; Brown et al., 2014; Morino et al., 2017). Some studies have argued for near-complete melting of the silicate Earth during the largest events (e.g., Rubie et al., 2011; Canup, 2012; Elkins-Tanton, 2012; Young et al., 2016). The pressures and temperatures near the bottom of such a deep magma ocean would have stabilized bridgmanite (Mg-perovskite), Ca-perovskite, and ferropericlase (e.g., Kato et al., 1988; Abe, 1997; Walter et al., 2004). Because REE and HFSE are variably compatible in Ca-perovskite, with the degree of compatibility decreasing in the order Lu > Hf > Sm > Nd (Corgne et al., 2005), the presence of Ca-perovskite on the liquidus in the lower mantle would result in much stronger fractionation of Lu/Hf than Sm/Nd. Over time, this would result in Nd-Hf isotopic decoupling in the mantle domains derived from crystallized magma ocean differentiation products.

In addition to the decoupling of the ^{143}Nd-^{176}Hf isotopic systems, early magma ocean silicate differentiation would be expected to have also resulted in fractionation of Hf from W and Sm from Nd, if this differentiation occurred within the first 50 and 500 Ma of the Solar System history, respectively. These fractionations, over time, would, in turn, have produced ^{182}W and ^{142}Nd anomalies in the magma ocean differentiation products. However, the μ^{182}W and μ^{142}Nd values in the Onega Basin rocks are BSE-like, arguing against such a scenario. Based on this argument, the hypothesis of recycling and long-term storage of Hadean mafic protocrust in the mantle can also be rejected as the mechanism for creating the Nd-Hf isotope decoupling.

Mixing of two melt batches with contrasting Nd-Hf isotopic compositions with highly contrasting Nd/Hf elemental ratios has been suggested to explain the common Nd-Hf isotopic decoupling observed in kimberlite suites. Tappe et al. (2011) made the case for West Greenland, building their argument on the Gaffney et al. (2007) study, and the subject of kimberlite Nd-Hf isotope decoupling was recently reviewed by Tappe et al. (2020b). However, unlike kimberlites, the rocks of the present study do not show any Nd-Hf isotope variations across the Onega Basin, which makes magma mixing not a viable hypothesis to explain the Nd-Hf isotopic decoupling in the source of these lavas.

The Lu-Hf and Sm-Nd isotope systems have been shown to be strongly decoupled by the terrestrial sedimentary cycle (e.g., Patchett et al., 1984; Vervoort et al., 1999; Garçon et al., 2013). This decoupling is caused by mechanical fractionation of zircon $(Zr,Hf)SiO_4$, a highly weathering-resistant mineral, during sediment transport, where zircon is preferentially deposited in coastal settings as coarse, heavy, sandy, terrigenous sediments characterized by extremely low Lu/Hf. These sediments are carried by turbidite currents onto the continental shelf and the upper part of the continental slope, while finer-grained, lighter pelagic sediments, depleted in zircon and, therefore, having high Lu/Hf, are carried over longer distances and eventually deposited in deep waters. Over time, these two types of sediments will acquire low and high initial εHf values, respectively, whereas the initial εNd values in both types of sediments will not be significantly affected by this process because sedimentary sorting does not fractionate neigboring REE such as Nd and Sm, but only REE and HFSE such as Lu and Hf. However, these upper crustal sedimentary rocks would also be characterized by strongly negative Nb/Nb* anomalies (e.g., McLennan, 2001; Rudnick and Gao, 2003, 2014), which would have been transferred to the Onega parental magmas, along with the decoupled Nd-Hf signature. Instead, the latter are characterized by highly positive Nb/Nb* anomalies. This observation, hence, allows us to exclude sedimentary input as the mechanism for creating the Nd-Hf decoupling in the Onega Basin magma source.

As evident from Fig. 5, the Onega Basin picrites are strikingly similar in both absolute and relative lithophile trace element abundances to recent plume-derived Hawaiian picrites, and, more specifically, to Kilauea and Loihi lavas (e.g., Norman and Garcia, 1999). They are also similar in terms of the initial Nd, Hf, and Pb isotopic compositions when corrected for the age of the lavas (e.g., Pietruszka et al., 2018; Ruttor et al., 2022). This may imply certain similarities in the mantle source composition and magma genesis between these ancient and modern OIB-type magmas.

Zindler and Hart (1986) and Hart et al. (1992) used Sr, Nd, and Pb isotopic data for MORB and OIB to identify five mantle endmembers: DMM, PREMA or FOZO, HIMU, EM1, and EM2. The last three endmembers are relatively rare and are considered to contain crustal materials, either oceanic crust in the case of HIMU or continental crust in the case of EM, recycled into the mantle (White and Hofmann, 1982). The PREMA component is isotopically depleted, with radiogenic ^{143}Nd and ^{176}Hf compositions and unradiogenic ^{87}Sr and ^{206}Pb compositions as a result of early melting and melt extraction (Hart et al., 1992). It has been postulated that mantle sources of many OIB contain various amounts of recycled crustal materials (HIMU, EM) and mantle domains that have been variously depleted via previous melt extraction episodes (DMM, PREMA).

Among OIB representing different mantle endmembers, aside from EM1 and EM2 lavas that show strong negative Nb/Nb* anomalies, the only types that exhibit deficits in initial εHf values relative to initial εNd values are those that are characterized by the presence of ancient recycled oceanic crust in their sources (Salters and White, 1998; Chauvel and Blichert-Toft, 2001; Lassiter et al., 2003; Chauvel et al., 2008). This is due to the fact that oceanic crust, generally thought to be represented by N-MORB, has suprachondritic ^{147}Sm/^{144}Nd, but subchondritic ^{176}Lu/^{177}Hf (Hofmann, 1988; Sun and McDonough, 1989). Consequently, over time, this disparity would result in strongly decoupled Nd-Hf systematics in the oceanic crust, with a deficit in initial εHf values relative to the corresponding εNd values. This decoupled Nd-Hf isotopic signature can be transferred to mantle plume sources of OIB originated from ancient subducted oceanic crust (Hofmann and White, 1982). To summarize, based on the Nd, Hf, and Pb isotopic data, the source of the Onega Basin lavas is most consistent with a PREMA-like composition containing a component of recycled oceanic crust.

5.5. Os isotope and HSE abundance systematics of the Onega source

The presence of ancient recycled oceanic crust in the sources of plume-derived oceanic basalts in general, and in the source of Hawaiian lavas in particular, has been widely accepted to explain their radiogenic ^{187}Os compositions (e.g., Walker et al., 1991, 1999; Hauri and Hart, 1993, 1997; Roy-Barman and Allègre, 1995; Widom, 1997; Lassiter and Hauri, 1998; Dale et al., 2007; Sobolev et al., 2008). This is due to the constrasting behavior of Re and Os during mantle melting, with Re being moderately incompatible and Os being compatible with the melting

residue. During the relatively low-degree partial melting (3–5 %) that is involved in the generation of basaltic magmas, these mafic melts would acquire high Re/Os ratios and the resulting oceanic crust would, over time, evolve to highly radiogenic ^{187}Os compositions. After being recycled back into the mantle, this oceanic crust may become entrained in the sources of mantle plumes that would then produce lavas with variably radiogenic ^{187}Os compositions. At the same time, the recycled component would have little impact on the ^{186}Os composition of the hybrid sources due to the much less incompatible behavior of Pt during mantle melting and the very long half-life and low atomic abundance of the parent isotope ^{190}Pt (Walker et al., 1997; Brandon et al., 1999; Puchtel and Humayun, 2000).

Here, we performed model calculations to evaluate the effects of oceanic crust recycling on the Os isotopic composition of the Onega Basin mantle source. For the purpose of the modeling, we considered two separate scenarios, whereby the oceanic crust was recycled 4.0 or 3.0 Ga ago; i.e., it sank, dehydrated, and aged for 2.0 or 1.0 Ga in the mantle before being entrained in the source of the Onega plume. For the HSE composition of the Archean oceanic crust, we adopted the model komatiite-basalt crust from the Puchtel and Humayun (2000) study. The results of the modeling are presented in Fig. 13. The calculations indicate that, depending on the residence time in the mantle, it would require between 10 and 20 % komatiite-basalt crust to be mixed into the Onega plume source to account for the radiogenic ^{187}Os signature of the Angozero picrites and Konchozero sill rocks. This result is similar to the amount of subducted oceanic crust in the source of the Hawaiian plume estimated to range from 10 to 20 % (Lassiter and Hauri, 1998; Sobolev et al., 2005) and is within the range of estimates for the amount of subducted oceanic crust in plume sources worldwide (i.e., between 2.0 and 20 %: Sobolev et al, 2007).

It has also been argued that, as a result of the dehydration reactions that accompany the downgoing slab, it may lose as much as 60 % of its Re inventory to hydrothermal fluids, with only a small effect on the Os abundances (e.g., Becker, 2000). This decrease in the Re/Os ratio would result in slower ingrowth of ^{187}Os in the subducted eclogitic slab and, as a result, would require a larger amount, between 20 and 30 %, of eclogitic crust in the Onega plume source to account for its radiogenic ^{187}Os composition (Fig. 13). Such a substantial amount of a mafic component in the Onega source would still be consistent with the major and trace element composition of the Onega parental magmas, although

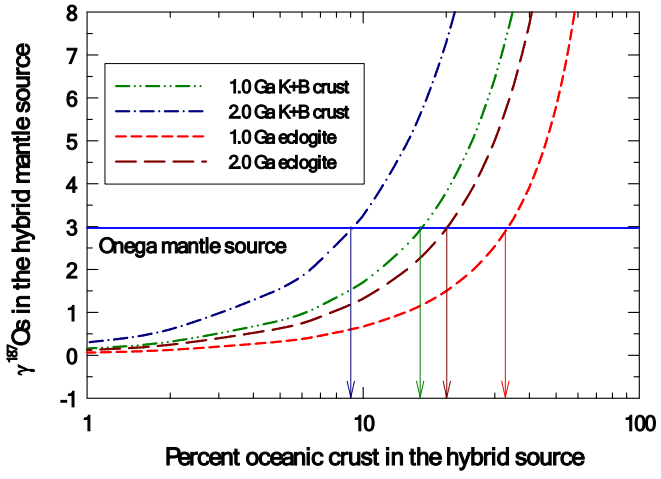

Fig. 13. Diagram illustrating the effects on the Os isotopic composition of incorporation into the source of the Onega plume of subducted Archean komatiite-basaltic oceanic crust that either retained its Re inventory (K + B crust) or lost 60 % of its Re inventory (eclogite) and aged for either 2.0 or 1.0 Ga in the mantle. The HSE composition of the Archean komatiite-basalt crust was adopted from Puchtel and Humayun (2000). See text for additional details of the model.

20 % appears to be a more realistic number. Additionally, the presence of 30 % eclogitic component in the Onega mantle source would make it very difficult for such mantle domain to buoyantly rise, unless it was extremely hot; such a hot mantle plume would be expected to produce komatiites and not relatively low-MgO picrites. Either way, if this estimate of the amount of oceanic crust present in the source of the Onega lavas is correct, it may imply an onset of some form of crustal recycling processes on Earth as early as 4.0 Ga ago based on the estimated residence times of the recycled oceanic crust in the mantle.

Despite the availability of high-precision Os isotopic data and apparent immobile behavior of HSE in the Onega picrites and Konchozero sill rocks during post-magmatic alteration, the absolute abundances of the HSE in the Onega source cannot be estimated quantitatively using the bootstrap protocol of Puchtel et al. (2004) that has been applied in prior studies of komatiites (e.g., Puchtel et al., 2022a and references therein). This is due to the apparently sulfide-saturated nature of the emplaced picritic magmas, as evident from the compatible behavior of essentially all HSE during differentiation of the picritic lavas and the mafic–ultramafic rocks of the sill (Fig. 8). The sulfide-saturated nature of the Onega picritic magmas was likely the result of the fractional crystallization processes that the parental picritic magma underwent *en route* to the surface and after emplacement. Nevertheless, the HSE abundances in the Angozero picrites can be compared qualitatively with picritic lavas with similar MgO content such as those from Hawaii (Ireland et al., 2009: Fig. 9). The Angozero picrites ($N = 8$) have, on average, similar concentrations of Os (~1 ppb), but a factor of 2 to 3 higher abundances of Ir, Ru, Pt, and Pd, compared to the Hawaiian picrites ($N = 53$). At the same time, the HSE abundances in the Angozero picrites are a factor of two to three lower than those in an average late Archean komatiite (Puchtel et al., 2022b; Puchtel and Arndt, 2025). These differences in the HSE abundances may be due to much lower degrees of partial melting for the Angozero picrites compared to komatiites, but somewhat higher than those involved in the formation of the Hawaiian picrites. They may also reflect differences in the HSE abundances in the mantle sources of the three groups of mafic–ultramafic rocks, or some combination of these factors.

5.6. *Implications for the evolution of the ^{182}W and ^{142}Nd composition of the mantle*

Our new and published ^{142}Nd and ^{182}W isotopic data for Archean and Proterozoic mafic–ultramafic rocks are plotted as a function of their crystallization ages in Fig. 14, together with the data for modern MORB and OIB. The majority of these rocks are represented by komatiites, which were likely derived from melting in mantle plumes that originated either at the core-mantle boundary, in the mantle transition zone (MTZ), or at the 670 km discontinuity (e.g., Wyman, 2020; Puchtel et al., 2022b; Puchtel and Arndt, 2025 and references therein), i.e., in the lower mantle, whereas non-plume magmas were likely derived from melting in the upper mantle. Therefore, the entire dataset may provide a good representation of the composition of the BSE for ^{142}Nd and ^{182}W.

In the diagram of μ^{182}W versus age (Fig. 14a), the new Onega Basin data represent an important reference point in that it partially fills the large gap between data for the recent and ancient rock records. When all the Archean and post-Archean komatiite-basalt data are considered, it is evident that there was a relatively gradual transition from dominantly anomalous, both ^{182}W-positive and ^{182}W-negative, mantle in the Archean, to a modern BSE-like mantle in the early Proterozoic, with the vertex located near the Archean-Proterozoic boundary at 2.5 Ga.

The Archean-Proterozoic boundary represents an important transition period in Earth history. It was likely characterized by rapid cooling of the mantle as manifested by a sharp decrease in both overall komatiite abundance and MgO contents of komatiitic magmas (e.g., Bickle, 1982, 1986; Nisbet et al., 1993; Herzberg et al., 2007, 2010). This shift may reflect fundamental changes in heat flux across the core-mantle boundary (e.g., Campbell and Griffiths, 1992, 2014), stabilization of

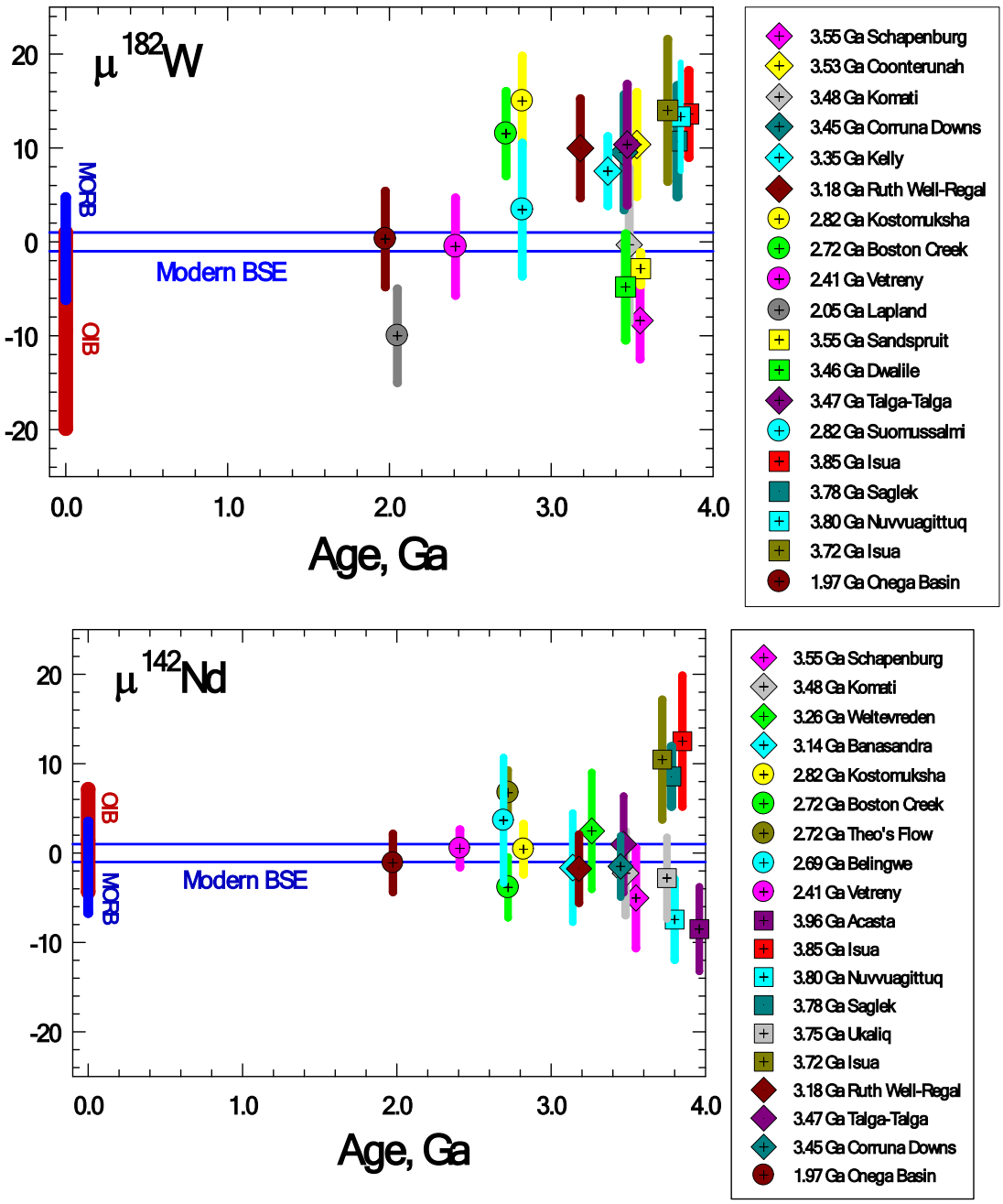

Fig. 14. $^{182}W/^{184}W$ (a) and $^{142}Nd/^{144}Nd$ (b) data obtained to date for mafic–ultramafic rocks worldwide. The colored bands represent the 2SD uncertainty on the mean μ ^{182}W and μ ^{142}Nd values for each locality. Data are from: 3.96 Ga Acasta – Roth et al. (2014), Reimink et al. (2018); 3.85 Ga Isua – Caro et al. (2006), Bennett et al. (2007), Rizo et al. (2013, 2016), Willbold et al. (2011), Dale et al. (2017), Saji et al. (2018), Tusch et al. (2019); 3.80 Ga Nuvvuagittuq – O'Neil et al. (2012), Touboul et al. (2014); 3.78 Ga Saglek – Liu et al. (2016), Morino et al. (2017, 2018); 3.75 Ga Ukaliq – Caro et al. (2017); 3.72 Ga Isua – Rizo et al. (2011, 2016), O'Neil et al. (2016), Tusch et al. (2019); 3.55 Ga Schapenburg – Puchtel et al. (2016a); 3.55 Ga Sandspruit – Tusch et al. (2022); 3.53 Ga Coonterunah – Tusch et al. (2021), Puchtel et al. (2022a); 3.48 Ga Komati and 3.26 Weltevreden – Touboul et al. (2012), Caro et al. (2006), Puchtel et al. (2013), Schneider et al. (2018), Boyet et al. (2021), Tusch et al. (2022); 3.47 Ga Talga-Talga – Tusch et al. (2021); 3.46 Dwalile – Tusch et al. (2022); 3.45 Ga Corruna Downs – Archer et al. (2019), Rizo et al. (2019), Murphy et al. (2021); 3.35 Ga Kelly – Tusch et al. (2021), Puchtel et al. (2022a); 3.18 Ga Ruth Well and Regal – Archer et al. (2019), Tusch et al. (2021), Puchtel et al. (2022a); 3.14 Ga Banasandra – Maya et al. (2017); 2.82 Ga Kostomuksha and 2.69 Ga Belingwe – Touboul et al. (2012), Boyet and Carlson (2006); 2.82 Ga Suomussalmi – Mei et al. (2023); 2.72 Ga Boston Creek – Puchtel et al. (2018); 2.72 Ga Theo's Flow – Debaille et al. (2013); 2.41 Ga Vetreny Belt – Puchtel et al. (2016b); 2.05 Ga Lapland – Puchtel et al. (2020); 1.97 Ga Onega Basin – this study; OIB – Caro et al. (2006), Andreasen et al. (2008), Murphy et al. (2010), Touboul et al. (2012), Mundl et al. (2017), Mundl-Petermeier et al. (2019, 2020), Rizo et al. (2019), Horan et al. (2018), Saji et al. (2018), Peters et al. (2018), Hyung and Jacobsen (2020); MORB – Caro et al. (2006), Mundl et al. (2017), Hyung and Jacobsen (2020), Peters et al. (2024).

major cratons (e.g., Condie and O'Neill, 2010), onset of modern-style plate tectonics (e.g., Brown and Johnson, 2018), or any combination of these processes.

Several authors have argued that the change from the ^{182}W-positive mantle in the Archean to a modern BSE-like mantle in the post-Archean and a ^{182}W-negative mantle in modern times was likely due to either influx of W with low μ^{182}W from the core into the lower mantle or isotopic exchange across the core-mantle boundary (e.g., Rizo et al., 2019; Mundl-Petermeier et al., 2020; Peters et al., 2021; Mei et al., 2023). The pattern observed in Fig. 14 would be consistent with such an

interpretation, but would also require an additional process to explain the simultaneous presence of both ^{182}W- and ^{142}Nd-negative mantle domains at 3.5–3.9 Ga and their near-complete disappearance by 2.5 Ga. This process would likely be a gradual homogenization of deep-seated mantle domains formed during crystallization of an early magma ocean. Such a gradual change in the heterogeneous W isotopic composition of the early Earth's mantle was likely facilitated by oceanic crust recycling processes, such as those revealed by the Onega Basin lavas. These recycling processes would provide a mechanism for effective convective whole-mantle mixing of the existing early isotopic heterogeneities in the mantle (e.g., Reimink et al., 2020; Tappe et al., 2020a; Nakanishi et al., 2023; Peters et al., 2024).

On the other hand, the new ^{142}Nd data for the Onega Basin rocks (Fig. 14b) provide further support to the notion that any significant ^{142}Nd isotopic heterogeneities that existed in the Archean mantle were largely homogenized by the end of the Archean (e.g., Debaille et al., 2013; Hyung and Jacobsen, 2020; Hyung et al., 2023).

6. Conclusions

(1) The emplaced Onega Basin picritic magmas feature moderate enrichments in LREE ($La/Sm_N = 1.5 \pm 0.2$), depletions in HREE ($Gd/Yb_N = 2.2 \pm 0.1$), positive Nb anomalies ($Nb/Nb^* = 1.6 \pm 0.1$), and BSE-like average $W/Th = 0.20 \pm 0.08$. Model calculations indicate that the parental picritic magmas were likely derived from 3 % equilibrium batch melting of a LREE-depleted garnet lherzolite PREMA-type mantle source containing a component of recycled oceanic crust.

(2) The Sm-Nd, Lu-Hf, and Re-Os combined whole-rock-mineral isochrons robustly constrain the timing of the Onega Basin picritic lava emplacement at ~1974 Ma. The initial $\varepsilon^{143}Nd = +3.0 \pm 0.5$ and $\varepsilon^{176}Hf = +2.8 \pm 1.2$ values derived from the respective isochrons indicate decoupling of the Nd and Hf isotope systems in the source of the picritic magmas. The initial $\mu^{186}Os$ and $\gamma^{187}Os$ values are suprachondritic at $+4.9 \pm 2.1$ and $+2.9 \pm 0.4$, respectively, indicating evolution of the Onega mantle source with time-integrated slightly suprachondritic Pt/Os and Re/Os ratios. These suprachondritic ratios, the Nd-Hf isotopic decoupling, and the observed trace element systematics can be accounted for by incorporation into the Onega Basin mantle source of 10–20 % recycled komatiite-basalt crust aged for 1 to 2 Ga in the mantle.

(3) The ^{142}Nd and ^{182}W compositions indicate modern BSE-like $\mu^{142}Nd = -1.1 \pm 3.3$ and $\mu^{182}W = 0.0 \pm 4.8$ in the mantle source of the Onega Basin lavas, providing new evidence that ^{142}Nd and ^{182}W anomalies had been well homogenized in the deep mantle by ~2.0 Ga. This was most likely due to the effects of enhanced whole-mantle mass and heat transport facilitated by processes of oceanic crust recycling that may have operated since at least the early Archean.

CRediT authorship contribution statement

Igor Puchtel: Conceptualization, Methodology, Formal Analysis, Investigation, Writing – Original Draft, Reviewing and Editing, Project Administration, Funding Acquisition. **Jan Hellmann:** Investigation, Formal Analysis, Writing – Reviewing and Editing. **Hanika Rizo:** Investigation, Formal Analysis, Writing – Reviewing and Editing, Funding Acquisition. **Janne Blichert-Toft:** Investigation, Formal Analysis, Writing – Reviewing and Editing. **Alexandra Stepanova:** Resources, Writing – Reviewing and Editing. **Alexander Samsonov:** Resources, Writing – Reviewing and Editing, Funding Acquisition. **Richard Walker:** Writing – Reviewing and Editing.

Data Availability

Data are available through Mendeley Data at https://doi.org/10.17632/m4ztbx6kcz.1.

Declaration of competing interest

The authors declare that they have no known competing financial interests or personal relationships that could have appeared to influence the work reported in this paper.

Acknowledgments

ISP acknowledges support from the United States National Science Foundation Petrology and Geochemistry grant EAR-2220936. HR acknowledges support from the Natural Sciences and Engineering Research Council of Canada grants RGPIN-2015-03982 and RGPIN-477144-2015. HR would like to thank Shuangquan Zhang for assistance with the TIMS and Jonathan O'Neil for support in the clean laboratories at the University of Ottawa. A.V. Stepanova and A.V. Samsonov acknowledge support from the Russian Science Foundation Project no. 23-17-00260. We thank Guillaume Caro, Sebastian Tappe, and Qing-Feng Mei for constructive criticism and useful suggestions that helped improve the manuscript, and Associate Editors Vinciane Debaille and Oliver Nebel for editorial handling.

Appendix A. Supplementary material

The Supplementary Material file contains (1) full details of the Analytical Techniques used in this study, (2) photomicrographs of the Konchozero sill rocks (Figure S1), (3) major element data for USGS GRM BIR-1 and BCR-1 (Table S1), (4) trace element data for USGS GRM BCR-1 and BIR-1 (Table S2), (5) Re-Os isotopic and HSE abundance data for GRM TDB-1, MUH-1, and OKUM (Table S3), (6) Sm-Nd isotope and abundance data for USGS GRM BIR-1 and BCR-1 (Table S4), (7) complete set of the high-precision Nd isotope data for JNdi standard and Angozero picrites and Konchohozero sill rocks (Table S5), and (8) complete set of the W isotope data obtained in this study (Table S6). Supplementary material to this article can be found online at https://doi.org/10.1016/j.gca.2025.01.013.

References

Abe, Y., 1997. Thermal and chemical evolution of the terrestrial magma ocean. Phys. Earth Planet. In. 100 (1–4), 27–39.

Andreasen, R., Sharma, M., Subbarao, K.V., Viladkar, S.G., 2008. Where on Earth is the enriched Hadean reservoir? Earth Planet. Sci. Lett. 266 (1–2), 14–28.

Archer, G.J., Mundl, A., Walker, R.J., Worsham, E.A., Bermingham, K.R., 2017. High-precision analysis of $^{182}W/^{184}W$ and $^{183}W/^{184}W$ by negative thermal ionization mass spectrometry: per-integration oxide corrections using measured $^{18}O/^{16}O$. Int. J. Mass Spectrom. 414, 80–86.

Archer, G.J., Brennecka, G.A., Gleißner, P., Stracke, A., Becker, H., Kleine, T., 2019. Lack of late-accreted material as the origin of ^{182}W excesses in the Archean mantle: Evidence from the Pilbara Craton, Western Australia. Earth Planet. Sci. Lett. 528, 115841.

Arzamastsev, A.A., Stepanova, A.V., Samsonov, A.V., Skuf'in, P.K., Salnikova, E.B., Larionov, A.N., Larionova, Y.O., Egorova, S.V., Erofeeva, K.G., 2020. Mafic Magmatism of Northeastern Fennoscandia (2.06-1.86 Ga): Geochemistry of Volcanic Rocks and Correlation with Dike Complexes. Stratigr. Geol. Correl. 28 (1), 1–34.

Becker, H., 2000. Re-Os fractionation in eclogites and blueschists and the implications for recycling of oceanic crust into the mantle. Earth Planet. Sci. Lett. 177 (3–4), 287–300.

Begemann, F., Ludwig, K.R., Lugmair, G.W., Min, K., Nyquist, L.E., Patchett, P.J., Renne, P.R., Shih, C.-Y., Villa, I.M., Walker, R.J., 2001. Call for an improved set of decay constants for geochronological use. Geochim. Cosmochim. Acta 65 (1), 111–121.

Bennett, V.C., Brandon, A.D., Nutman, A.P., 2007. Coupled ^{142}Nd-^{143}Nd isotopic evidence for Hadean mantle dynamics. Science 318 (5858), 1907–1910.

Bickle, M.J., 1982. The magnesium contents of komatiitic liquids. In: Arndt, N.T., Nisbet, E.G. (Eds.), Komatiites. George Allen and Unwin, London, pp. 479–494.

Bickle, M.J., 1986. Implications of melting for stabilisation of lithosphere and heat loss in the Archaean. Earth Planet. Sci. Lett. 80 (3–4), 314–324.

Bizimis, M., Griselin, M., Lassiter, J.C., Salters, V.J.M., Sen, G., 2007. Ancient recycled mantle lithosphere in the Hawaiian plume: Osmium-Hafnium isotopic evidence from peridotite mantle xenoliths. Earth Planet. Sci. Lett. 257 (1–2), 259–273.
Blichert-Toft, J., 2001. On the Lu-Hf isotope geochemistry of silicate rocks. Geostandards Newsletter-J. Geostandards Geoanalysis 25 (1), 41–56.
Blichert-Toft, J., Albarède, F., 1997. The Lu-Hf isotope geochemistry of chondrites and the evolution of the mantle-crust system. Earth Planet. Sci. Lett. 148 (1–2), 243–258.
Blichert-Toft, J., Chauvel, C., Albaréde, F., 1997. Separation of Hf and Lu for high-precision isotope analysis of rock samples by magnetic sector multiple collector ICP-MS. Contrib. Miner. Petrol. 127 (3), 248–260.
Blichert-Toft, J., Frey, F.A., Albarède, F., 1999. Hf isotope evidence for pelagic sediments in the source of Hawaiian basalts. *Science* 285, 879–882.
Blichert-Toft, J., Boyet, M., Telouk, P., Albarede, F., 2002. ^{147}Sm-^{143}Nd and ^{176}Lu-^{176}Hf in eucrites and the differentiation of the HED parent body. Earth Planet. Sci. Lett. 204 (1–2), 167–181.
Blichert-Toft, J., Puchtel, I.S., 2010. Depleted mantle sources through time: evidence from Lu-Hf and Sm-Nd isotope systematics of Archean komatiites. Earth Planet. Sci. Lett. 297 (3–4), 598–606.
Blichert-Toft, J., Arndt, N.T., Wilson, A., Coetzee, G., 2015. Hf and Nd isotope systematics of early Archean komatiites from surface sampling and ICDP drilling in the Barberton Greenstone Belt, South Africa. Am. Mineral. 100, 2396–2411.
Bottke, W.F., Walker, R.J., Day, J.M.D., Nesvorny, D., Elkins-Tanton, L., 2010. Stochastic Late Accretion to Earth, the Moon, and Mars. Science 330 (6010), 1527–1530.
Bouvier, A., Vervoort, J.D., Patchett, P.J., 2008. The Lu-Hf and Sm-Nd isotopic composition of CHUR: Constraints from unequilibrated chondrites and implications for the bulk composition of terrestrial planets. Earth Planet. Sci. Lett. 273 (1–2), 48–57.
Boyet, M., Carlson, R.W., 2006. A new geochemical model for the Earth's mantle inferred from ^{146}Sm-^{142}Nd systematics. Earth Planet. Sci. Lett. 250 (1–2), 254–268.
Boyet, M., Blichert-Toft, J., Rosing, M., Storey, M., Télouk, P., Albarède, F., 2003. ^{142}Nd evidence for early Earth differentiation. Earth Planet. Sci. Lett. 214 (3–4), 427–442.
Boyet, M., Garçon, M., Arndt, N.T., Carlson, R.W., Konc, Z., 2021. Residual liquid from deep magma ocean crystallization in the source of komatiites from the ICDP drill core in the Barberton Greenstone Belt. Geochim. Cosmochim. Acta 304, 141–159.
Brandon, A.D., Norman, M.D., Walker, R.J., Morgan, J.W., 1999. ^{186}Os-^{187}Os systematics of Hawaiian picrites. Earth Planet. Sci. Lett. 174 (1–2), 25–42.
Brandon, A.D., Walker, R.J., Puchtel, I.S., 2006. Platinum-osmium isotope evolution of the Earth's mantle: Constraints from chondrites and Os-rich alloys. Geochim. Cosmochim. Acta 70 (8), 2093–2103.
Brown, S.M., Elkins-Tanton, L.T., Walker, R.J., 2014. Effects of magma ocean crystallization and overturn on the development of ^{142}Nd and ^{182}W isotopic heterogeneities in the primordial mantle. Earth Planet. Sci. Lett. 408, 319–330.
Brown, M., Johnson, T., 2018. Secular change in metamorphism and the onset of global plate tectonics. Am. Mineral. 103 (2), 181–196.
Budde, G., Archer, G.J., Tissot, F.L.H., Tappe, S., Kleine, T., 2022. Origin of the analytical ^{183}W effect and its implications for tungsten isotope analyses. J. Anal. At. Spectrom 37 (10), 2005–2021.
Campbell, I.H., Griffiths, R.W., 1992. The changing nature of mantle hotspots through time: implications for the chemical evolution of the mantle. J. Geol. 92 (5), 497–523.
Campbell, I.H., Griffiths, R.W., 2014. Did the formation of D" cause the Archaean-Proterozoic transition? Earth Planet. Sci. Lett. 388, 1–8.
Canup, R.M., 2012. Forming a Moon with an Earth-like Composition via a Giant Impact. Science 338 (6110), 1052–1055.
Caro, G., Bourdon, B., Birck, J.-L., Moorbath, S., 2003. ^{146}Sm-^{142}Nd evidence from Isua metamorphosed sediments for early differentiation of the Earth's mantle. Nature 423 (6938), 428–432.
Caro, G., Bourdon, B., Wood, B.J., Corgne, A., 2005. Trace-element fractionation in Hadean mantle generated by melt segregation from a magma ocean. Nature 436 (7048), 246–249.
Caro, G., Bourdon, B., Birck, J.-L., Moorbath, S., 2006. High-precision ^{142}Nd/^{144}Nd measurements in terrestrial rocks: constraints on the early differentiation of the Earth's mantle. Geochim. Cosmochim. Acta 70 (1), 164–191.
Caro, G., Morino, P., Mojzsis, S.J., Cates, N.L., Bleeker, W., 2017. Sluggish Hadean geodynamics: evidence from coupled ^{146,147}Sm-^{142,143}Nd systematics in Eoarchean supracrustal rocks of the Inukjuak domain (Québec). Earth Planet. Sci. Lett. 457, 23–37.
Chauvel, C., Blichert-Toft, J., 2001. A hafnium isotope and trace element perspective on melting of the depleted mantle. Earth Planet. Sci. Lett. 190 (3–4), 137–151.
Chauvel, C., Lewin, E., Carpentier, M., Arndt, N.T., Marini, J.-C., 2008. Role of recycled oceanic basalt and sediment in generating the Hf-Nd mantle array. Nat. Geosci. 1 (1), 64–67.
Condie, K.C., O'Neill, C., 2010. The Archean-Proterozoic Boundary: 500 My of Tectonic Transition in Earth History. Am. J. Sci. 310 (9), 775–790.
Cook, D.L., Schönbächler, M., 2016. High-precision measurement of W isotopes in Fe–Ni alloy and the effects from the nuclear field shift. J. Anal. At. Spectrom 31 (7), 1400–1405.
Corgne, A., Liebske, C., Wood, B.J., Rubie, D.C., Frost, D.J., 2005. Silicate perovskite-melt partitioning of trace elements and geochemical signature of a deep perovskitic reservoir. Geochim. Cosmochim. Acta 69 (2), 485–496.
Creaser, R.A., Papanastassiou, D.A., Wasserburg, G.J., 1991. Negative thermal ion mass-spectrometry of Osmium, Rhenium, and Iridium. Geochim. Cosmochim. Acta 55 (1), 397–401.
Dale, C.W., Gannoun, A., Burton, K.W., Argles, T.W., Parkinson, I.J., 2007. Rhenium-osmium isotope and elemental behaviour during subduction of oceanic crust and the implications for mantle recycling. Earth Planet. Sci. Lett. 253 (1–2), 211–225.
Dale, C.W., Kruijer, T.S., Burton, K.W., 2017. Highly siderophile element and ^{182}W evidence for a partial late veneer in the source of 3.8 Ga rocks from Isua, Greenland. Earth Planet. Sci. Lett. 458, 394–404.
Debaille, V., O'Neill, C., Brandon, A.D., Haenecour, P., Yin, Q.-Z., Mattielli, N., Treiman, A.H., 2013. Stagnant-lid tectonics in early Earth revealed by ^{142}Nd variations in late Archean rocks. Earth Planet. Sci. Lett. 373, 83–92.
Elkins-Tanton, L.T., 2012. Magma Oceans in the Inner Solar System. Annu. Rev. Earth Planet. Sci. 40 (1), 113–139.
Elkins-Tanton, L.T., Parmentier, E.M., Hess, P.C., 2003. Magma ocean fractional crystallization and cumulate overturn in terrestrial planets: Implications for Mars. Meteorit. Planet. Sci. 38 (12), 1753–1771.
Elthon, D., Scarfe, C.H., 1984. High-pressure phase equilibria of a high-magnesia basalt and the genesis of primary oceanic basalts. Am. Mineral. 69 (1–2), 1–15.
Foley, S.F., Barth, M.G., Jenner, G.A., 2000. Rutile/melt partition coefficients for trace elements and an assessment of the influence of rutile on the trace element characteristics of subduction zone magmas. Geochim. Cosmochim. Acta 64 (5), 933–938.
Gaál, G., Gorbatschev, R., 1987. An outline of the Precambrian evolution of the Baltic Shield. Precambr. Res. 35, 15–52.
Gaffney, A.M., Blichert-Toft, J., Nelson, B.K., Bizzarro, M., Rosing, M., Albarede, F., 2007. Constraints on source-forming processes of West Greenland kimberlites inferred from Hf-Nd isotope systematics. Geochim. Cosmochim. Acta 71 (11), 2820–2836.
Garcia, V.B., O'Neil, J., Dantas, E.L., 2023. Rare evidence for the existence of a Hadean enriched mantle reservoir. Geochem. Perspect. Lett. 28, 1–6.
Garçon, M., Boyet, M., Carlson, R.W., Horan, M.F., Auclair, D., Mock, T.D., 2018. Factors influencing the precision and accuracy of Nd isotope measurements by thermal ionization mass spectrometry. Chem. Geol. 476, 493–514.
Hamilton, P.J., O'Nions, R.K., Bridgwater, D., Nutman, A.P., 1983. Sm-Nd studies of Archaean metasediments and metavolcanics from West Greenland and their implications for the Earth's early history. Earth Planet. Sci. Lett. 62 (2), 263–272.
Hanski, E.J., Smolkin, V.F., 1989. Pechenga ferropicrites and other Early Proterozoic picrites in the eastern part of the Baltic Shield. Precambr. Res. 45 (1–3), 63–82.
Hanski, E.J., Smolkin, V.F., 1995. Iron- and LREE-enriched mantle source for early Proterozoic intraplate magmatism as examplified by the Pechenga ferropicrites, Kola Peninsula, Russia. Lithos 34 (1–3), 107–126.
Hanski, E.J., Huhma, H., Smolkin, V.F., Vaasjoki, M., 1990. The age of ferropicritic volcanism and comagmatic Ni-bearing intrusions at Pechenga, Kola Peninsula, USSR. Bull. Geol. Soc. Finl. 62 (2), 123–133.
Hanski, E.J., 1992. Petrology of the Pechenga ferropicrites and cogenetic, Ni-bearing gabbro-wherlite intrusions, Kola Peninsula, Russia. Geological Survey of Finland Bulletin 367, 192 pp.
Harper, C.L., Jacobsen, S.B., 1992. Evidence from coupled ^{147}Sm-^{143}Nd and ^{146}Sm-^{142}Nd systematics for very early (4.5-Gyr) differentiation of the Earth's mantle. Nature 360, 728–732.
Hart, S.R., Hauri, E.H., Oschmann, L.A., Whitehead, J.A., 1992. Mantle plumes and entrainment: isotopic evidence. Science 256 (5056), 517–520.
Hauri, E.H., Hart, S.R., 1993. Re-Os isotope systematics of HIMU and EMII oceanic island basalts from the south Pacific Ocean. Earth Planet. Sci. Lett. 114 (2–3), 353–371.
Hauri, E.H., Hart, S.R., 1997. Rhenium abundances and systematics in oceanic basalts. Chem. Geol. 139 (1–4), 185–205.
Herzberg, C., Asimow, P.D., Arndt, N.T., Niu, Y.L., Lesher, C.M., Fitton, J.G., Cheadle, M. J., Saunders, A.D., 2007. Temperatures in ambient mantle and plumes: Constraints from basalts, picrites, and komatiites. Geochem. Geophys. Geosyst. 8, Q02006.
Herzberg, C., Condie, K., Korenaga, J., 2010. Thermal history of the Earth and its petrological expression. Earth Planet. Sci. Lett. 292 (1–2), 79–88.
Hofmann, A.W., 1988. Chemical differentiation of the Earth: the relationship between mantle, continental crust and oceanic crust. Earth Planet. Sci. Lett. 90 (3), 297–314.
Hofmann, A.W., Jochum, K.P., 1996. Source characteristics derived from very incompatible trace elements in Mauna Loa and Mauna Kea basalts, Hawaii Scientific Drilling Project. J. Geophys. Res. 101 (B5), 11831–11839.
Horan, M.F., Walker, R.J., Morgan, J.W., Grossman, J.N., Rubin, A.E., 2003. Highly siderophile elements in chondrites. Chem. Geol. 196 (1–4), 5–20.
Horan, M.F., Carlson, R.W., Walker, R.J., Jackson, M., Garçon, M., Norman, M., 2018. Tracking Hadean processes in modern basalts with 142-Neodymium. Earth Planet. Sci. Lett. 484, 184–191.
Hyung, E., Ibañez-Mejia, M., Rojas-Agramonte, Y., 2023. The survival of tracers of primordial mantle heterogeneity investigated through ^{142}Nd/^{144}Nd and ^{3}He/^{4}He isotope decoupling in the Gorgona Island lavas. Earth Planet. Sci. Lett. 622, 118409.
Hyung, E., Jacobsen, S.B., 2020. The ^{142}Nd/^{144}Nd variations in mantle-derived rocks provide constraints on the stirring rate of the mantle from the Hadean to the present. Proc. Natl. Acad. Sci. 117 (26), 14738–14744.
Hyung, E., Huang, S., Petaev, M.I., Jacobsen, S.B., 2016. Is the mantle chemically stratified? Insights from sound velocity modeling and isotope evolution of an early magma ocean. Earth Planet. Sci. Lett. 440, 158–168.
Ireland, T.J., Walker, R.J., Garcia, M.O., 2009. Highly siderophile element and 187Os isotope systematics of Hawaiian picrites: Implications for parental melt composition and source heterogeneity. Chem. Geol. 260 (1–2), 112–128.
Jacobsen, S.B., Harper, C.L., 1996. Accretion and Early Differentiation History of the Earth Based on Extinct Radionuclides. In: Earth Processes: Reading the Isotopic Code. Geophysical Monograph 95. American Geophysical Union, pp. 47–74.
Jacobsen, S.B., Wasserburg, G.J., 1980. Sm-Nd isotopic evolution of chondrites. Earth Planet. Sci. Lett. 50 (1), 139–155.
Jochum, K.P., Arndt, N.T., Hofmann, A.W., 1991. Nb-Th-La in komatiites and basalts: constraints on komatiite petrogenesis and mantle evolution. Earth Planet. Sci. Lett. 107 (2), 272–289.

Kato, T., Ringwood, A.E., Irifune, T., 1988. Experimental determination of element partitioning between silicate perovskite, garnet and liquid: constraints on early differentiation of the mantle. Earth Planet. Sci. Lett. 89 (1), 123–145.
Kinzler, R.J., Grove, T.L., 1985. Crystallization and differentiation of Archean komatiite lavas from northeast Ontario: Phase equilibrium and kinetic studies. Am. Mineral. 70 (1–2), 40–51.
Kleine, T., Mezger, K., Palme, H., Münker, C., 2004. The W isotope evolution of the bulk silicate Earth: constraints on the timing and mechanisms of core formation and accretion. Earth Planet. Sci. Lett. 228 (1–2), 109–123.
Kruijer, T.S., Kleine, T., 2018. No ^{182}W excess in the Ontong Java Plateau source. Chem. Geol. 485, 24–31.
Kruijer, T.S., Sprung, P., Kleine, T., Leya, I., Burkhardt, C., Wieler, R., 2012. Hf–W chronometry of core formation in planetesimals inferred from weakly irradiated iron meteorites. Geochim. Cosmochim. Acta 99, 287–304.
Labrosse, S., Hernlund, J.W., Coltice, N., 2007. A crystallizing dense magma ocean at the base of the Earth's mantle. Nature 450 (7171), 866–869.
Lassiter, J.C., Hauri, E.H., 1998. Osmium-isotope variations in Hawaiian lavas: evidence for recycled oceanic lithosphere in the Hawaiian plume. Earth Planet. Sci. Lett. 164 (3–4), 483–496.
Lassiter, J.C., Blichert-Toft, J., Hauri, E.H., Barsczus, H.G., 2003. Isotope and trace element variations in lavas from Raivavae and Rapa, Cook-Austral islands: constraints on the nature of HIMU- and EM-mantle and the origin of mid-plate volcanism in French Polynesia. Chem. Geol. 202 (1–2), 115–138.
Lee, D.C., Halliday, A.N., 1995. Hafnium-tungsten chronometry and the timing of terrestrial core formation. Nature 378 (6559), 771–774.
Lee, D.C., Halliday, A.N., 1996. Hf-W isotopic evidence for rapid accretion and differentiation in the early Solar system. Science 274 (5294), 1876–1879.
Liu, J., Touboul, M., Ishikawa, A., Walker, R.J., Pearson, D.G., 2016. Widespread tungsten isotope anomalies and W mobility in crustal and mantle rocks of the Eoarchean Saglek Block, northern Labrador, Canada: Implications for early Earth processes and W recycling. Earth Planet. Sci. Lett. 448, 13–23.
Ludwig, K.R., 2003. ISOPLOT 3.00. A geochronological toolkit for Microsoft Excel. Berkeley Geochronology Center Spec. Publ. No. 4, 70 pp.
Lugmair, G.W., Marti, K., 1978. Lunar initial ^{143}Nd/^{144}Nd: Differential evolution of the lunar crust and mantle. Earth Planet. Sci. Lett. 39 (3), 349–357.
Marchi, S., Canup, R.M., Walker, R.J., 2018. Heterogeneous delivery of silicate and metal to the Earth by large planetesimals. Nat. Geosci. 11, 77–81.
Maya, J.M., Bhutani, R., Balakrishnan, S., Rajee Sandhya, S., 2017. Petrogenesis of 3.15 Ga old Banasandra komatiites from the Dharwar craton, India: Implications for early mantle heterogeneity. Geosci. Front. 8 (3), 467–481.
McLennan, S.M., 2001. Relationships between the trace element composition of sedimentary rocks and upper continental crust. Geochem. Geophys. Geosyst. 2 (4), 2000GC000109.
Mei, Q.-F., Yang, J.-H., Wang, Ya.-F., Wang, H., Peng, P., 2020. Tungsten isotopic constraints on homogenization of the Archean silicate Earth: Implications for the transition of tectonic regimes. Geochim. Cosmochim. Acta 278, 51–64.
Mei, Q.-F., Yang, J.-H., Li, C.-F., Wang, X.-C., Konnunaho, J., Wu, Y.-D., Zhong, H., Xu, Y.-G., Wang, H., 2023. Modern ocean island basalt-like ^{182}W signature in Paleoarchean mafic rocks: implications for the generation, preservation, and destruction of early mantle heterogeneities. Geology 51 (10), 519–523.
Meissner, F., Schmidt-Ott, W.D., Ziegeler, L., 1987. Half-life and α-ray energy of ^{146}Sm. Zeitschrift Für Physik A Atomic Nuclei 327 (2), 171–174.
Melezhik, V.A., Prave, A.R., Hanski, E.J., Fallick, A.E., Lepland, A., Kump, L.R., Strauss, H., 2013. The Palaeoproterozoic of Fennoscandia as Context for the Fennoscandian Arctic Russia - Drilling Early Earth Project. In: Reading the Archive of Earth's Oxygenation. Springer-Verlag, Berlin-Heidelberg, 495 pp.
Mertzman, S.A., 2000. K-Ar results from the southern Oregon - northern California Cascade range. Or. Geol. 62 (4), 99–122.
Morino, P., Caro, G., Reisberg, L., Schumacher, A., 2017. Chemical stratification in the post-magma ocean Earth inferred from coupled ^{146,147}Sm-^{142,143}Nd systematics in ultramafic rocks of the Saglek block (3.25-3.9 Ga; northern Labrador, Canada). Earth Planet. Sci. Lett. 463, 136–150.
Morino, P., Caro, G., Reisberg, L., 2018. Differentiation mechanisms of the early Hadean mantle: Insights from combined ^{176}Hf-^{142,143}Nd signatures of Archean rocks from the Saglek Block. Geochim. Cosmochim. Acta 240, 43–63.
Mundl, A., Touboul, M., Jackson, M.G., Day, J.M.D., Kurz, M.D., Lekic, V., Helz, R.T., Walker, R.J., 2017. Tungsten-182 heterogeneity in modern ocean island basalts. Science 356 (6333), 66–69.
Mundl-Petermeier, A., Walker, R.J., Jackson, M.G., Blichert-Toft, J., Kurz, M.D., Haldórsson, S.A., 2019. Temporal evolution of primordial tungsten-182 and ^{3}He/^{4}He signatures in the Iceland mantle plume. Chem. Geol. 525, 245–259.
Mundl-Petermeier, A., Walker, R.J., Fischer, R.A., Lekic, V., Jackson, M.G., Kurz, M.D., 2020. Anomalous μ^{182}W signatures in high ^{3}He/^{4}He ocean island basalts – fingerprints of Earth's core? Geochim. Cosmochim. Acta 271, 194–211.
Murphy, D.T., Brandon, A.D., Debaille, V., Burgess, R., Ballentine, C., 2010. In search of a hidden long-term isolated sub-chondritic ^{142}Nd/^{144}Nd reservoir in the deep mantle: Implications for the Nd isotope systematics of the Earth. Geochim. Cosmochim. Acta 74 (2), 738–750.
Murphy, D., Rizo, H., O'Neil, J., Hepple, R., Wiemer, D., Kemp, A., Vervoort, J., 2021. Combined Sm-Nd, Lu-Hf, and ^{142}Nd study of Paleoarchean basalts from the East Pilbara Terrane, Western Australia. Chem. Geol. 578, 120301.
Nakanishi, N., Giuliani, A., Carlson, R.W., Horan, M.F., Woodhead, J., Pearson, D.G., Walker, R.J., 2021. Tungsten-182 evidence for an ancient kimberlite source. Proc. Natl. Acad. Sci. 118 (23), e2020680118.
Nakanishi, N., Puchtel, I.S., Walker, R.J., Nabelek, P.I., 2023. Dissipation of Tungsten-182 Anomalies in the Archean Upper Mantle: Evidence from the Black Hills, South Dakota, USA. Chem. Geol. 617, 121255.
Nicklas, R.W., Puchtel, I.S., Ash, R.D., Piccoli, P.M., Hanski, E., Nisbet, E.G., Waterton, P., Pearson, D.G., Anbar, A.D., 2019. Secular mantle oxidation across the Archean-Proterozoic boundary: Evidence from V partitioning in komatiites and picrites. Geochim. Cosmochim. Acta 250, 49–75.
Nisbet, E.G., Cheadle, M.J., Arndt, N.T., Bickle, M.J., 1993. Constraining the potential temperature of the Archaean mantle: a review of the evidence from komatiites. Lithos 30, 291–307.
Norman, M.D., Garcia, M.O., 1999. Primitive magmas and source characteristics of the Hawaiian plume: petrology and geochemistry of shield picrites. Earth Planet. Sci. Lett. 168 (1–2), 27–44.
Norman, M., Garcia, M.O., Pietruszka, A.J., 2005. Trace-element distribution coefficients for pyroxenes, plagioclase, and olivine in evolved tholeiites from the 1955 eruption of Kilauea Volcano, Hawai'i, and petrogenesis of differentiated rift-zone lavas. Am. Mineral. 90 (5–6), 888–899.
O'Neil, J., Carlson, R.W., Paquette, J.-L., Francis, D., 2012. Formation age and metamorphic history of the Nuvvuagittuq Greenstone Belt. Precambr. Res. 220–221, 23–44.
O'Neil, J., Rizo, H., Boyet, M., Carlson, R.W., Rosing, M.T., 2016. Geochemistry and Nd isotopic characteristics of Earth's Hadean mantle and primitive crust. Earth Planet. Sci. Lett. 442, 194–205.
Patchett, P.J., Kauvo, O., Hedge, C.E., Tatsumoto, M., 1981. Evolution of continental crust and mantle heterogeneity: evidence from Hf isotopes. Contrib. Miner. Petrol. 78 (3), 279–297.
Patchett, P.J., White, W.M., Feldmann, H., Kielinczuk, S., Hofmann, A.W., 1984. Hafnium/rare earth element fractionation in the sedimentary system and crustal recycling into the Earth's mantle. Earth Planet. Sci. Lett. 69 (2), 365–378.
Peters, B.J., Carlson, R.W., Day, J.M.D., Horan, M.F., 2018. Hadean silicate differentiation preserved by anomalous ^{142}Nd/^{144}Nd ratios in the Réunion hotspot source. Nature 555, 89–106.
Peters, B.J., Mundl-Petermeier, A., Carlson, R.W., Walker, R.J., Day, J.M.D., 2021. Combined lithophile-siderophile isotopic constraints on Hadean processes preserved in ocean island basalt sources. Geochem. Geophys. Geosyst. 22 (3), e2020GC009479.
Peters, D., Rizo, H., O'Neil, J., Hamelin, C., Shirey, S.B., 2024. Comparative ^{142}Nd and ^{182}W study of MORBs and the 4.5 Gyr evolution of the upper mantle. Geochem. Perspect. Lett. 29, 51–56.
Pietruszka, A.J., Norman, M.D., Garcia, M.O., Marske, J.P., Burns, D.H., 2013. Chemical heterogeneity in the Hawaiian mantle plume from the alteration and dehydration of recycled oceanic crust. Earth Planet. Sci. Lett. 361, 298–309.
Pietruszka, A.J., Marske, J.P., Heaton, D.E., Garcia, M.O., Rhodes, J.M., 2018. An Isotopic Perspective into the Magmatic Evolution and Architecture of the Rift Zones of Kilauea Volcano. J. Petrol. 59 (12), 2311–2352.
Puchtel, I.S., Arndt, N.T., Hofmann, A.W., Haase, K.M., Kröner, A., Kulikov, V.S., Kulikova, V.V., Garbe-Schönberg, C.-D., Nemchin, A.A., 1998. Petrology of mafic lavas within the Onega plateau, central Karelia: Evidence for 2.0 Ga plume-related continental crustal growth in the Baltic Shield. Contrib. Miner. Petrol. 130 (2), 134–153.
Puchtel, I.S., Arndt, N.T., 2025. Archean to recent komatiites and basalts. In: Chauvel, C. (Ed.), Treatise on Geochemistry, 3Rd Edition, Chapter 00065. Elsevier, Amsterdam, p. 40.
Puchtel, I.S., Brügmann, G.E., Hofmann, A.W., 1999. Precise Re-Os mineral isochron and Pb-Nd-Os isotope systematics of a mafic-ultramafic sill in the 2.0 Ga Onega plateau (Baltic Shield). Earth Planet. Sci. Lett. 170 (4), 447–461.
Puchtel, I.S., Humayun, M., 2000. Platinum group elements in Kostomuksha komatiites and basalts: Implications for oceanic crust recycling and core-mantle interaction. Geochim. Cosmochim. Acta 64 (24), 4227–4242.
Puchtel, I.S., Humayun, M., Campbell, A., Sproule, R., Lesher, C.M., 2004. Platinum group element geochemistry of komatiites from the Alexo and Pyke Hill areas, Ontario. Canada. Geochimica et Cosmochimica Acta 68 (6), 1361–1383.
Puchtel, I.S., Blichert-Toft, J., Touboul, M., Walker, R.J., Byerly, G., Nisbet, E.G., Anhaeusser, C.R., 2013. Insights into early Earth from Barberton komatiites: Evidence from lithophile isotope and trace element systematics. Geochim. Cosmochim. Acta 108, 63–90.
Puchtel, I.S., Blichert-Toft, J., Touboul, M., Horan, M.F., Walker, R.J., 2016a. The coupled ^{182}W-^{142}Nd record of early terrestrial mantle differentiation. Geochem. Geophys. Geosyst. 17 (6), 2168–2193.
Puchtel, I.S., Touboul, M., Blichert-Toft, J., Walker, R.J., Brandon, A.D., Nicklas, R.W., Kulikov, V.S., Samsonov, A.V., 2016b. Lithophile and siderophile element systematics of the mantle at the Archean-Proterozoic boundary: Evidence from 2.4 Ga komatiites. Geochim. Cosmochim. Acta 180, 227–255.
Puchtel, I.S., Blichert-Toft, J., Touboul, M., Walker, R.J., 2018. ^{182}W and HSE constraints from 2.7 Ga komatiites on the heterogeneous nature of the Archean mantle. Geochim. Cosmochim. Acta 228, 1–26.
Puchtel, I.S., Mundl-Petermeier, A., Horan, M., Hanski, E.J., Blichert-Toft, J., Walker, R. J., 2020. Ultra-depleted 2.05 Ga komatiites of Finnish Lapland: Products of grainy late accretion or core-mantle interaction? Chem. Geol. 554, 119801.
Puchtel, I.S., Nicklas, R.W., Slagle, J., Horan, M., Walker, R.J., Nisbet, E.G., Locmelis, M., 2022a. Early global mantle chemical and isotope heterogeneity revealed by the komatiite-basalt record: The Western Australia connection. Geochim. Cosmochim. Acta 320, 238–278.
Puchtel, I.S., Blichert-Toft, J., Horan, M.F., Touboul, M., Walker, R.J., 2022b. The komatiite testimony to ancient mantle heterogeneity. Chemical Geology, Invited Review Paper 594, 120776.

Reimink, J.R., Chacko, T., Carlson, R.W., Shirey, S.B., Liu, J., Stern, R.A., Bauer, A.M., Pearson, D.G., Heaman, L.M., 2018. Petrogenesis and tectonics of the Acasta Gneiss Complex derived from integrated petrology and ^{142}Nd and ^{182}W extinct nuclide-geochemistry. Earth Planet. Sci. Lett. 494, 12–22.

Reimink, J.R., Mundl-Petermeier, A., Carlson, R.W., Shirey, S.B., Walker, R.J., Pearson, D.G., 2020. Tungsten isotope composition of Archean crustal reservoirs and implications for terrestrial μ^{182}W evolution. Geochem. Geophys. Geosyst. 21 (7), e2020GC009155.

Ren, Z.-Y., Hanyu, T., Miyazaki, T., Chang, Q., Kawabata, H., Takahashi, T., Hirahara, Y., Nichols, A.R.L., Tatsumi, Y., 2009. Geochemical Differences of the Hawaiian Shield Lavas: Implications for Melting Process in the Heterogeneous Hawaiian Plume. J. Petrol. 50 (8), 1553–1573.

Rizo, H., Boyet, M., Blichert-Toft, J., Rosing, M., 2011. Combined Nd and Hf isotope evidence for deep-seated source of Isua lavas. Earth Planet. Sci. Lett. 312 (3–4), 267–279.

Rizo, H., Boyet, M., Blichert-Toft, J., Rosing, M.T., 2013. Early mantle dynamics inferred from 142Nd variations in Archean rocks from southwest Greenland. Earth Planet. Sci. Lett. 377–378, 324–335.

Rizo, H., Walker, R.J., Carlson, R.W., Touboul, M., Horan, M.F., Puchtel, I.S., Boyet, M., Rosing, M.T., 2016. Early Earth differentiation investigated through ^{142}Nd, ^{182}W, and highly siderophile element abundances in samples from Isua, Greenland. Geochim. Cosmochim. Acta 175, 319–336.

Rizo, H., Andrault, D., Bennett, N.R., Humayun, M., Brandon, A.D., Vlastelic, I., Moine, B., Poirier, A., Bouhifd, M.A., Murphy, D.T., 2019. ^{182}W evidence for core-mantle interaction in the source of mantle plumes. Geochem. Perspect. Lett. 11, 6–11.

Roth, A.S.G., Bourdon, B., Mojzsis, S.J., Rudge, J.F., Guitreau, M., Blichert-Toft, J., 2014. Combined ^{147,146}Sm-^{143,142}Nd constraints on the longevity and residence time of early terrestrial crust. Geochem. Geophys. Geosyst. 15 (6), 2329–2345.

Roy-Barman, M., Allègre, C.-J., 1995. ^{187}Os/^{186}Os in oceanic island basalts: tracing oceanic crust recycling in the mantle. Earth Planet. Sci. Lett. 129 (1–4), 145–161.

Rubie, D.C., Frost, D.J., Mann, U., Asahara, Y., Nimmo, F., Tsuno, K., Kegler, P., Holzheid, A., Palme, H., 2011. Heterogeneous accretion, composition and core-mantle differentiation of the Earth. Earth Planet. Sci. Lett. 301 (1–2), 31–42.

Rudnick, R.L., Gao, S., 2003. Composition of the Continental Crust. In: Treatise on Geochemistry, first ed., Elsevier, Amsterdam, vol. 3, pp. 1-64.

Rudnick, R.L., Barth, M., Horn, I., McDonough, W.F., 2000. Rutile-bearing refractory eclogites: missing link between continents and depleted mantle. Science 287 (5451), 278–281.

Rudnick, R.L., Gao, S., 2014. Composition of the Continental Crust. In: Treatise on Geochemistry, second ed. Elsevier, Amsterdam, pp. 1–51.

Ruttor, S., Nebel, O., Nebel-Jacobsen, Y., Norman, M.D., Kendrick, M.A., Rogers, A., Mather, B.R., 2022. Iron isotope systematics during igneous differentiation in lavas from Kilauea and Mauna Loa, Hawai'I. Chem. Geol. 606, 120973.

Saji, N.S., Larsen, K., Wielandt, D., Schiller, M., Costa, M.M., Whitehouse, M.J., Rosing, M.T., Bizzarro, M., 2018. Hadean geodynamics inferred from time-varying ^{142}Nd/^{144}Nd in the early Earth rock record. Geochem. Perspect. Lett. 7, 43–48.

Salters, V.J.M., White, W.M., 1998. Hf isotope constraints on mantle evolution. Chem. Geol. 145 (3–4), 447–460.

Scherer, E., Münker, C., Mezger, K., 2001. Calibration of the lutetium-hafnium clock. Science 293 (5530), 683–687.

Schneider, K.P., Hoffmann, J.E., Boyet, M., Münker, C., Kröner, A., 2018. Coexistence of enriched and modern-like ^{142}Nd signatures in Archean igneous rocks of the eastern Kaapvaal Craton, southern Africa. Earth Planet. Sci. Lett. 487, 54–66.

Schoenberg, R., Kamber, B.S., Collerson, K.D., Eugster, O., 2002. New W-isotope evidence for rapid terrestrial accretion and very early core formation. Geochim. Cosmochim. Acta 66 (17), 3151–3160.

Shirey, S.B., Walker, R.J., 1998. The Re-Os isotope system in cosmochemistry and high-temperature geochemistry. Annual Rev. Earth Planetary Sci. 26, 423–500.

Smoliar, M.I., Walker, R.J., Morgan, J.W., 1996. Re-Os ages of Group IIA, IIIA, IVA, and IVB iron meteorites. Science 271 (5762), 1099–1102.

Sobolev, A.V., Hofmann, A.W., Sobolev, S.V., Nikogosian, I.K., 2005. An olivine-free mantle source of Hawaiian shield basalts. Nature 433 (7033), 590–597.

Sobolev, A.V., Hofmann, A.W., Kuzmin, D.V., Yaxley, G.M., Arndt, N.T., Chung, S.L., Danyushevsky, L.V., Elliott, T., Frey, F.A., Garcia, M.O., Gurenko, A.A., Kamenetsky, V.S., Kerr, A.C., Krivolutskaya, N.A., Matvienkov, V.V., Nikogosian, I. K., Rocholl, A., Sigurdsson, I.A., Sushchevskaya, N.M., Teklay, M., 2007. The amount of recycled crust in sources of mantle-derived melts. Science 316 (5823), 412–417.

Sobolev, A.V., Hofmann, A.W., Brügmann, G., Batanova, V.G., Kuzmin, D.V., 2008. A Quantitative Link Between Recycling and Osmium Isotopes. Science 321, 536.

Söderlund, U., Patchett, J.P., Vervoort, J.D., Isachsen, C.E., 2004. The ^{176}Lu decay constant determined by Lu-Hf and U-Pb isotope systematics of Precambrian mafic intrusions. Earth Planet. Sci. Lett. 219 (3–4), 311–324.

Sokolov, V.A., 1987. Geology of Karelia. Nauka, Leningrad, p. 232.

Stalder, R., Foley, S.F., Brey, G.P., Horn, I., 1998. Mineral aqueous fluid partitioning of trace elements at 900-1200°C and 3.0-5.7 GPa: New experimental data for garnet, clinopyroxene, and rutile, and implications for mantle metasomatism. Geochim. Cosmochim. Acta 62 (10), 1781–1801.

Stepanova, A.V., Samsonov, A.V., Arzamastsev, A.A., Larionov, A.N., Larionova, Y.O., 2024. Age Limits for the Zaonega Formation of the Ludicovian Superhorizon and the Shunga Event in the Onega Basin: New U-Pb Zircon Data for the Konchezero Sill. Dokl. Earth Sci. 515 (2), 624–631.

Sun, S.-S., McDonough, W.F., 1989. Chemical and isotopic systematics of oceanic basalts: Implications for mantle composition and processes. In: Saunders, A.D., Norry, M.J. (Eds.), Magmatism in the Ocean Basins, No. 42. Geological Society Special Publication, pp. 313–345.

Svetov, A.P., 1979. The Platform Basaltic Volcanism in Karelia. Nauka, Leningrad, p. 208.

Tappe, S., Pearson, D.G., Nowell, G.M., Nielsen, T.F.D., Milstead, P., Muehlenbachs, K., 2011. A fresh isotopic look at Greenland kimberlites: Cratonic mantle lithosphere imprint on deep source signal. Earth Planet. Sci. Lett. 305, 235–248.

Tappe, S., Budde, G., Stracke, A., Wilson, A., Kleine, T., 2020a. The tungsten-182 record of kimberlites above the African superplume: Exploring links to the core-mantle boundary. Earth Planet. Sci. Lett. 547, 116473.

Tappe, S., Stracke, A., van Acken, D., Strauss, H., Luguet, A., 2020b. Origins of kimberlites and carbonatites during continental collision – insights beyond decoupled Nd-Hf isotopes. Earth Sci. Rev. 208, 103287.

Tonks, W.B., Melosh, H.J., 1993. Magma Ocean Formation Due to Giant Impacts. J. Geophys. Res. 98 (E3), 5319–5333.

Touboul, M., Puchtel, I.S., Walker, R.J., 2012. ^{182}W Evidence for Long-Term Preservation of Early Mantle Differentiation Products. Science 335, 1065–1069.

Touboul, M., Liu, J., O'Neil, J., Puchtel, I.S., Walker, R.J., 2014. New Insights into the Hadean Mantle Revealed by ^{182}W and Highly Siderophile Element Abundances of Supracrustal Rocks from the Nuvvuagittuq Greenstone Belt, Quebec, Canada. Chem. Geol. 383, 63–75.

Tusch, J., Sprung, P., van de Löcht, J., Hoffmann, J.E., Boyd, A.J., Rosing, M.T., Münker, C., 2019. Uniform ^{182}W isotope compositions in Eoarchean rocks from the Isua region, SW Greenland: the role of early silicate differentiation and missing late veneer. Geochim. Cosmochim. Acta 257, 284–310.

Tusch, J., Münker, C., Hasenstab, E., Jansen, M., Marien, C.S., Kurzweil, F., Van Kranendonk, M.J., Smithies, H., Maier, W., Garbe-Schönberg, D., 2021. Convective isolation of Hadean mantle reservoirs through Archean time. Proc. Natl. Acad. Sci. 118 (2), e2012626118.

Tusch, J., Hoffmann, J.E., Hasenstab, E., Fischer-Gödde, M., Marien, C.S., Wilson, A.H., Münker, C., 2022. Long-term preservation of Hadean protocrust in Earth's mantle. Proc. Natl. Acad. Sci. 119 (18), e2120241119.

Vervoort, J.D., Blichert-Toft, J., 1999. Evolution of the depleted mantle: Hf isotope evidence from juvenile rocks through time. Geochim. Cosmochim. Acta 63 (3–4), 533–556.

Vervoort, J.D., Patchett, P.J., Blichert-Toft, J., Albarède, F., 1999. Relationships between Lu-Hf and Sm-Nd isotopic systems in the global sedimentary system. Earth Planet. Sci. Lett. 168 (1–2), 79–99.

Vervoort, J.D., Patchett, P.J., Albarède, F., Blichert-Toft, J., Rudnick, R., Downes, H., 2000. Hf-Nd isotopic evolution of the lower crust. Earth Planet. Sci. Lett. 181 (1–2), 115–129.

Vockenhuber, C., Oberli, F., Bichler, M., Ahmad, I., Quitté, G., Meier, M., Halliday, A.N., Lee, D.C., Kutschera, W., Steier, P., Gehrke, R.J., Helmer, R.G., 2004. New Half-Life Measurement of ^{182}Hf: Improved Chronometer for the Early Solar System. Phys. Rev. Lett. 93 (17), 172501.

Völkening, J., Koppe, M., Heumann, K.G., 1991. Tungsten Isotope Ratio Determinations by Negative Thermal Ionization Mass-Spectrometry. Int. J. Mass Spectrom. Ion Process. 107 (2), 361–368.

Walker, R.J., Echeverria, L.M., Shirey, S.B., Horan, M.F., 1991. Re-Os isotopic constraints on the origin of volcanic rocks, Gorgona Island, Colombia: Os-isotopic evidence for ancient heterogeneities in the mantle. Contrib. Miner. Petrol. 107 (2), 150–162.

Walker, R.J., Morgan, J.W., Beary, E.S., Smoliar, M.I., Czamanske, G.K., Horan, M.F., 1997. Applications of the ^{190}Pt-^{186}Os isotope system to geochemistry and cosmochemistry. Geochim. Cosmochim. Acta 61 (22), 4799–4807.

Walker, R.J., Storey, M., Kerr, A.C., Tarney, J., Arndt, N.T., 1999. Implications of ^{187}Os isotopic heterogeneities in a mantle plume: Evidence from Gorgona Island and Curaçao. Geochim. Cosmochim. Acta 63 (5), 713–728.

Walter, M.J., Nakamura, E., Trønnes, R.G., Frost, D.J., 2004. Experimental constraints on crystallization differentiation in a deep magma ocean. Geochim. Cosmochim. Acta 68 (20), 4267–4284.

White, W.M., Hofmann, A.W., 1982. Sr and Nd isotope geochemistry of oceanic basalts and mantle evolution. Nature 296 (5860), 821–825.

Widom, E., 1997. Sources of ocean island basalts: a review of the osmium isotope evidence. Physica A 244 (1–4), 484–496.

Willbold, M., Stracke, A., 2006. Trace element composition of mantle end-members: Implications for recycling of oceanic and upper and lower continental crust. Geochem. Geophys. Geosyst. 7 (4), Q04004.

Willbold, M., Elliott, T., Moorbath, S., 2011. The tungsten isotopic composition of the Earth's mantle before the terminal bombardment. Nature 477 (7363), 195–198.

Wyman, D., 2020. Komatiites From Mantle Transition Zone Plumes. Front. Earth Sci. 8 (383), 540744.

Yin, Q., Jacobsen, S.B., Yamashita, K., Blichert-Toft, J., Telouk, P., Albarede, F., 2002. A short timescale for terrestrial planet formation from Hf-W chronometry of meteorites. Nature 418 (6901), 949–952.

Young, E.D., Kohl, I.E., Warren, P.H., Rubie, D.C., Jacobson, S.A., Morbidelli, A., 2016. Oxygen isotopic evidence for vigorous mixing during the Moon-forming giant impact. Science 351 (6272), 493–496.

Zindler, A., Hart, S.R., 1986. Chemical Geodynamics. Annual Rev. Earth Planetary Sci. 14, 493–571.